N° Ordre...../FT/UMBB/2021

REPUBLIQUE ALGERIENNE DEMOCRATIQUE ET POPULAIRE

MINISTERE DE L'ENSEIGNEMENT SUPERIEUR ET DE LA RECHERCHE SCIENTIFIQUE

UNIVERSITE M'HAMED BOUGARA-BOUMERDES

Faculté de Technologie

Thèse de Doctorat

Présentée par

FEKHAR Mustafa

En vue de l'obtention du diplôme de **DOCTORAT** en **LMD**

Filière : Mechanical engineering

Option : Mechanics and Engineering Systems

EFFECTS OF DENSITY ON COAXIAL SWIRLING JETS CHARACTERISTICS

Devant le jury composé de :

M. NOUR	Abdelkader	Professeur	UMBB	Président
M. BENKOUSSAS	Bouzid	Professeur	ENP(Alger)	Examinateur
M. ZAHLOUL	Hamou	Professeur	UHBC	Examinateur
M. MANSOURI	Kacem	Professeur	UMBB	Examinateur
M. SACI	Rachid	Professeur	UMBB	Directeur de thèse

Année Universitaire 2021/2022

Abstract

Thermal buoyancy, induced by injection or by differential heating of a rod, is explored to control breakdown onset which occurs in the core of a helical flow driven by the lid rotation of a vertical cylinder. Three main parameters are required to characterize numerically the flow behavior; namely, the rotational Reynolds number Re, the cavity aspect ratio Λ_h and the Richardson number Ri. Warm injection/rod, $Ri > 0$, is shown to prevent on-axis flow stagnation while breakdown enhancement is evidenced when $Ri < 0$. In addition, when $Ri > 0$, results revealed that a bubble vortex evolves into a ring type structure which may remain robust, as observed in prior related experiments or, in contrast, disappear over a given range of parameters $(\Lambda_h, Re, Ri > 0)$. Besides, the emergence of such a toroidal mode was not found to occur under thermal stratification induced by a differentially heated rod. Moreover, three state diagrams were established which provided detailed flow characteristics under the distinct and combined effects of buoyancy strength, viscous effects and cavity aspect ratio.

Keywords: Breakdown, Buoyancy, Cylinder, Injection, Rotating lid, differential heating

Résumé

La flottabilité, induite par injection ou par chauffage différentiel d'une tige, est adoptée comme moyen de control de l'apparition du phénomène d'éclatement au sein du noyau d'un écoulement hélicoïdal, engendré par la rotation du disque supérieur d'un cylindre vertical. Trois paramètres sont requis pour caractériser numériquement la structuration de l'écoulement ; en l'occurrence, le nombre de Reynolds Re, le rapport d'aspect de la cavité Λ_h et le nombre de Richardson Ri. Il découle qu'un jet/tige chaud, $Ri>0$ élimine la stagnation axiale alors que le cas $Ri<0$ la favorise. En outre, les résultats révèlent qu'un vortex de type bulle se détache de l'axe et évolue vers une structure toroidale qui peut demeurer stable, en accord avec l'expérience, ou au contraire disparaitre pour une plage donnée de paramètres $(\Lambda_h, Re, Ri>0)$. Par ailleurs, l'émergence du mode toroidal n'a pas été observée dans le cas de la stratification thermique induite par le chauffage différentiel d'une tige. De plus, trois diagrammes de stabilité ont été établis, qui fournissent des caractéristiques détaillées de l'écoulement sous l'influence de la variation distincte et combinée de la flottabilité, des effets visqueux et du rapport d'aspect de la cavité.

Mots clés: Eclatement, flottabilité, cylindre, injection, couvercle en rotation, chauffage différentiel.

ملخص

يتم استكشاف الطفو الحراري، الناجم عن طريق الحقن أو التسخين التفاضلي لقضيب، للتحكم في بداية الدوامات التي تحدث في قلب التدفق الحلزوني الذي يحركه دوران غطاء الأسطوانة العمودية. مطلوب ثلاث معلمات رئيسية لتوصيف سلوك التدفق عدديًا ؛ وهي رقم رينولدز Re الدوراني ونسبة أبعاد التجويف Λ_h ورقم ريتشاردسون Ri. يظهر الحقن / القضيب الدافئ $Ri > 0$ لمنع ركود التدفق على المحور بينما يتضح تعزيز الانهيار عندما $Ri < 0$. بالإضافة إلى ذلك، عندما كشفت النتائج أن دوامة الفقاعة تتطور إلى بنية من النوع الدائري والتي قد تظل قوية، كما لوحظ في التجارب السابقة ذات الصلة أو على النقيض من ذلك، تختفي عبر نطاق معين من المعلمات $(\Lambda_h, Re, Ri > 0)$. إلى جانب ذلك، لم يتم العثور على ظهور مثل هذا الوضع الحلقي تحت التقسيم الطبقي الحراري الناجم عن التسخين المحوري. علاوة على ذلك، تم إنشاء ثلاثة مخططات الحالة، والتي قدمت خصائص تدفق مفصلة تحت التأثيرات المتميزة والمجمعة لقوة الطفو وتأثيرات اللزوجة ونسبة أبعاد التجويف.

الكلمات المفتاحية: الانهيار ، الطفو ، الأسطوانة ، الحقن ، الغطاء الدوار ، التسخين التفاضلي

*This thesis has been supported by the **Dynamics motors and vibroacoustics Laboratory, Faculty of technology,** University **M'HAMED BOUGARA Boumerdes.***

*I first would like to acknowledge and give my warmest thanks to my supervisor, Professor **Rachid SACI,** who made this work possible. I am indebted to him for his patience, understanding, continued guidance and endless supply of advises and knowledge. His commitment to research and science is a source of inspiration.*

*I am also sincerely thankful to Professor **Abdelkader NOUR,** head of the Dynamics motors and vibroacoustics Laboratory, who kindly accepted to chair this thesis defense, despite his very busy time.*

*My thanks are also extended to all the comity members; namely, professor **Bouzid BENKOUSSAS**, Professor **Kacem MANSOURI**, and finally professor **Hamou ZAHLOUL**, for kindly accepting to examine the thesis and making very valuable comments and suggestions.*

*Special thanks are expressed to **Dr. Malika IMOULA,** for her interest and valuable assistance throughout the preparation of this research work; especially the numerical part.*

Finally, all those who contributed, directly or indirectly, to the accomplishment of this work, are warmly acknowledged.

Firstly, I want to thank Allah who guided me on the right track.

I am deeply indebted to my parents for all the steps of achievements and success I have accomplished in my whole life. Words cannot express enough their huge sacrifices. I pray Allah to protect them and wish them good health, happiness and a wonderful life.

My warm and heartfelt thanks go to my wife for her unfailing support and tremendous understanding; standing by me, with continuous encouragements which kept me hopeful and boosted my motivation. To her I say: Your prayers for me was what sustained me this far.

Obviously, to my lovely children Redouane and Arinas who shared the ups and downs, I wish them happiness and success for the future.

To my grand mother, whose prayers gave me tremendous motivation and good inspiration, I wish her very good health , happiness and long life.

To all my brothers and sisters,
To my uncles, aunts and all their relatives,
I pray Allah to grant them long life and good health

Finally, thanks to all my fellow students and friends without distinction: they are numerous and cannot list them, but can never forget them.

F. Mustafa

Contents

Abstract…… i

Résumé…… ii

ملخص…… iii

Acknowledgements……..iv

Didications……... v

Contents…….. vi

List of figures…….. ix

Nomenclature…… xiv

GENERALINTRODUCTION…… ……. 1

CHAPTER I INTRODUCTION AND LITERATURE SURVEY

I.1. Background ……5

I.2. Breakdown in Swirling jets ……6

I.2.1. Non swirling free jets ……6

I.2.2. swirling free jets ……7

I.2.3. Co-axial swirling jets ……...11

I.3. Breakdown in a confined medium ……...14

I.4. Selected studies on vortex flows control ……...18

I.5. Theories and criteria for vortex breakdown ……...23

I.5.1. Theories based on hydrodynamic instability ……...23

I.5.2. Theories based on deceleration of axial flow leading to stagnation (criterion of Brown and Lopez [4]) ……...24

I.5.3. Theories based on transition from one flow state to another ……....24

I.6. Conclusion ……...26

I.7. Chapter references ……...27

CHAPTER II MATHEMATICAL FORMULATION

II.1. Introduction ……..……... 34

II.2. Physical model and formulation ……...34

II.3. Equations of motion (tensor form) ……...35

II.3.1. Dimensional form of the equations ……...36

II.3.2. Dimensionless form of the equations and control parameters ……36

II.3.3. Control parameters ……...38

II.3.4. Stream function-vorticity formulation ……...39

II.3.5. Initial and Boundary conditions ……...39

A. Configuration under injection ……...40

- Initial conditions…….. 40
- Boundary conditions which apply for all times $(0 \le t \le t_f)$ ..……40

B. Rod configuration ……...40

II.4. Conclusion ……...41

CHAPTER III THE NUMERICAL METHOD OF SOLUTION

III.1. Introduction ……...43

III.2. Numerical domain ……...44

III.3. Grid generation ……...45

III.4. Numerical procedure ……...46

III.5. Data Processing ……...47

III.6. Validation ……...47

III.6.1. Validation in the case of a configuration without injection ……47

III.7. Conclusion ……...49

III.8. Chapter references ……...50

CHAPTER IV SENSITIVITY OF ISOTHERMAL SWIRLING FLOWS TO DENSITY VARIATIONS

IV.1. Introduction ……...53

IV.2. Basic isothermal flow without injection ……...53

IV.3. The configuration with neutral injection (iso-density case) ……56

IV.4. Positively buoyant injection $(\Delta\rho/\rho_a = (\rho_j - \rho_a)/\rho_a > 0)$ ……58

IV.5. Negatively buoyant injection $(\Delta\rho/\rho_a = (\rho_j - \rho_a)/\rho_a < 0)$ ……60

IV.6. Conclusion ……...63

IV.7. Chapter references ……...64

CHAPTER V EFFECT OF THERMAL BUOYANCY ON CONFINED VORTEX FLOWS

V.1. Introduction ……...66

V.2. Geometry and control parameters ……...66

- Control parameters ……...66

V.3. Basic flow under neutrally buoyant injection ……67

V.4. Effect of thermally buoyant injection ……...68

V.4.1. Warm injection ……...68

- Combined effect of parameters $(Re, Ri > 0)$ ……...71

V.4.2. Cool injection ……..72

V.4.3. The role of the axial pressure ……...73

V.4.4. $(Re, Ri > 0)$ and (Re, Ri) state diagrams ……...74

V.4.5. The role of the local swirl number ……...76

V.5. The rod configuration under differential heating ……77

V.6. Conclusion ……...80

V.7. Chapter references ……...81

GENERAL CONCLUTION…… …… 89

List of figures

Figure I.1: selected vortex illustrations: Environmental vortex (tornado) [AMNH] and vortex in external flows (over an aircraft wings (aerodynamics)) [9]…… 5

Figure I.2: Schematic of a swirling jet components…… 6

Figure I.3: schematic of the structure of an axisymmetric free jet: (a) non-swirling jet; (b) swirling jet [14]…… 8

Figure I.4: Primary and secondary vortex flows over a delta wing; (a) schematic model and (b) Direct numerical Simulation [ONERA]…… 9

Figure I.5: swirling jet displaying: (a) bubble (b) spiral and (c) double helix breakdown visualized by instantaneous streaklines deduced by direct numerical simulations [19]…….. 10

Figure I.6: Flow visualization of an asymmetric cone type of breakdown in a free swirling jet; $Re = 606$ (Reynolds number), $S = 1.37$ (swirl number) [18]……..... 11

Figure I.7: schematic of the characteristics of two co-flowing streams with variable physical properties. In particular, the co-axial jet stagnation point location [20]….. 12

Figure I.8: (a) Schematic of a swirl burner [23] **(b)** Visualization of swirl burner with separate axial fuel injection into a premixed flame [21] **(c)** Illustration of a recirculation zone at the exit of the burner (a) [23]…… 13

Figure I.9: Mixing co-flow nozzle [24]……. 14

Figure I.10: (a) Sketch of a cylindrical enclosure with rotating bottom disk including the flow direction and the numerical domain which displays a bubble type breakdown **(b)** meridian ring (toroidal) type vortices driven by exact co-rotation of both end disks [25]; **(a')** axial velocity profile **(b')** velocity distribution at mid-depth…… 15

Figure I.11: a sketch of the topological patterns in the meridional plane [26]; Single centered VB, two coalescent VB, two and three ring type mid-plane

bubbles (exact co-rotation of both end wall), two on-axis VB……. 16

Figure I.12: laser cross-section of vortex breakdown structures at Λ=2.5for different Reynolds numbers. Flow images were captured using florescent dye [27……..….. 16

Figure I.13: Vortex breakdown structures at $Re = 1900$ for different aspect ratios. Flow images were captured using food dye [27……..…… 17

Figure I.14: Regions of breakdown onset and flow regimes: current results under isodensity injection ($distinct \times$ symbols) added for comparison to detailed stability diagrams supplied by Iwatsu et al. (absence of injection) [31…….….. 18

Figure I.15: combined effects of thermal buoyancy (Ri) (Richardson number) and rotational Reynolds number (Re) on the form of breakdown which occurs at the axis of a swirling jet under hot $(Ri < 0)$ /cold $(Ri > 0)$ axial injection, obtained by PIV measurements [48]…….. 20

Figure I.16: state diagram mapping regions of ring type (▼) and bubble type breakdown under the variation of Re and density ratio [49]: **(a)** configuration under light dye injection, **(b)** configuration under heavy dye injection…… 21

Figure I. 17: dye visualization of the vortex structure obtained by tilting slightly the top rotating disk; $Re = 1000$ and the tilt angle $(\alpha \sim 5°)$ [52]……..... 22

Figure I. 18: schematic of the transition flow states according to the theory of Escudier and Keller [60]…….. 25

Figure II.1: Schematic of the cylindrical enclosure adopted……. 35

Figure III.1: (Top) Schematic of the geometry and (bottom right) numerical domain which displays a meridian streamline pattern with a typical on-axis two bubble type breakdown and selected vortex characteristics referred to in section 3.1 : Z_s (upstream stagnation point), $e_{\max}$ (bubble radial extent), stagnation line $\psi = 0$, and the maximum volumetric flow rates inside ($\psi_{\min} < 0$) and outside ($\psi_{max} > 0$) the vortex. (Bottom left) the rod configuration…… 44

Figure III.2: Flow structure driven by the rotating bottom disk: Re = 1850 experiments by Escudier (image at the left)[13] compared to the present numerical

predictions (streamlines)…… 48

Figure III.3: Flow structure driven by the top rotating disk (Re=1850 Iwatsu [14]) which captures better the second bubble ; the right figure is sketch of the corresponding vortex characteristics……... 48

Figure IV.1: Contour plots of meridian streamlines (right) compared with experimental visualization [8]; $Re = 1850$, $\Lambda_h = 2$, iso-thermal and iso-density configuration without injection. Contour values are $\psi = \psi_{max}\,(i/10)^3, \psi_{min}\,(i/10)^3,\ i = 1....10$ …… 54

Figure IV.2: Schematic of the numerical meridian plane illust-rating two on-axis bubble type breakdown and the corresponding selected vortex characteristics…… 55

Figure IV.3: Close up of the vicinity of breakdown under isodensity injection $(0.5 < r < 0.5, 0 < z < 1.5)$; (a) before injection (b) experiments [3] (under injection) (c) after injection $Re = 2060$ …….. 56

Figure IV.4: Effect of iso-density injection on the axial velocity distribution along the cavity axis…….. 57

Figure IV.5: Regions of breakdown onset and flow regimes: current results under isodensity injection ($distinct \times$ symbols) added for comparison to detailed stability diagrams supplied by Iwatsu et al. (absence of injection) [8]…… 58

Figure IV.6: $(Re, \Delta\rho/\rho_a > 0)$ state diagram mapping the region of vortex breakdown (VB) occurrence under effect of heavy dye injection. Solid curves are the bounding curves predicted numerically and (□) Symbols denote the corresponding experimental results [3]…… 59

Figure IV.7: Close up of the steady reverse flow region under effect of negatively buoyant injection $(\rho_j < \rho_a)$; $Re = 1700,\ \Lambda_h = 1.98$ (steady case)…… 61

Figure IV.8: Schematic of the process of formation of vortex ring under light dye injection [12]……..…. 61

Figure IV.9: $(Re,\ \Delta\rho/\rho_a<0)$ state diagram, mapping regions of bubble (○) and ring type (▲) vortices under very light dye injection. In contrast to [3], breakdown is suppressed in region with square (□) symbols. (*): region which lacks breakdown...62

Figure V.1: Schematic of the geometry and numerical domain which displays a meridian streamline pattern with an on-axis two bubble type breakdown and selected vortex characteristics : Z_s (upstream stagnation point), $e_{\max}$ (bubble radial extent), stagnation line $\psi=0$ maximum volumetric flow rates inside ($\psi_{\min}<0$) and outside ($\psi_{max}>0$) the vortex…….. 67

Figure V.2: A close up of an on-axis vortex (solid lignes) in the meridian plane $[0,r[\times[0,z[$. (left) no injection and (right) under isothermal injection. P_s and P_r are the upstream and downstream stagnation points respectively…….. 68

Figure V.3: A ring type vortex induced by warm injection (meridian streamlines at the right) and experimental dye visualization (left) [3];
$(Re,\Lambda_h,Ri)=(2423,1.98,0.023)$ ……. 69

Figure V.4: (a), (b), (c): flow pattern under effect of warm injection; $Re=1700$, $\Lambda_h=1.98$ for three selected values of Ri as indicated above; (a'), (b'), (c') : a close up of the corresponding reverse flow regions respectively……. 71

Figure V.5: $(Re,Ri>0)$ diagram for two selected times. As Ri increases vortex breakdown (VB) evolves into a toroidal pattern which may remain observable or disappear…….. 72

Figure V.6: Meridian streamlines illustrating effects of cool injection $(Ri<0)$;
$(Re,\Lambda_h,Ri)=(1700,1.98,-0.023)$ ……..… 73

Figure V.7: Distribution of the pressure coefficient on the cavity axis corresponding to the steady flow pattern induced for $Re=1700,\ \Lambda_h=1.98$ …… 74

Figure V.8: (Re,Λ_h) Diagram mapping the breakdown region (bounded by an upper and lower curve) for three selected $Ri<0$ values. Cool injection enhances breakdown……....75

Figure V.9: (Re, Ri) diagram for five aspect ratios, indicating breakdown occurrence under warm $(Ri > 0)$ and cool $(Ri < 0)$ injection: for $\Lambda_h = 1$ and $\Lambda_h = 1.3$ breakdown bounded by an upper and lower curve while for higher aspect ratios it occurs above a single curve (breakdown threshold)..... 76

Figure V.10: Radial distribution of the velocity field at $z_m = 0.26$ corresponding to the configuration $\mathrm{Re} = 2060$, $\Lambda_h = 2.5$, $Ri = 0.023$ (solid curves) and $Ri = 0$ (broken curves)..... 77

Figure V.11: Meridian flow pattern subjected to differentially heated/cooled rod; $Re = 1700, \Lambda_h = 1.98$ 79

Figure V.12: Axial velocity distribution corresponding to the critical Ri required to suppress breakdown: $Ri = 0.116$ (rod case) and $Ri = 0.046$ (injection case); $Re = 1700$, $\Lambda_h = 1.98$ 80

Nomenclature

$e_{\max}$: maximum radial extent of a bubble

H : cavity height (m)

h : rod height (m)

R : cavity radius (m)

R_o : radius of the orifice (m)

R_r : rod radius (m)

r^* :dimensionless radius $r^* = \frac{r}{R}$

Re : rotational Reynolds number

Re_c : critical rotational Reynolds number

Ri : Richardson number

T_a : ambient temperature (K)

T_j : inlet temperature (K)

T_r : reference temperature (K)

U_j : inlet injection velocity ($mm.s^{-1}$)

T_{rod} : rod temperature (K)

Z_s : stagnation point location

z^* :dimensionless height $z^* = \frac{z}{H}$

β : thermal expansion coefficient (K^{-1})

ΔT : temperature gradient (K)

δ_h : rod aspect ratio

δ_r : rod radius ratio

δ_o : orifice radius ratio

δt : time step

Γ : angular momentum (circulation)

Λ_h : cavity aspect ratio

ρ_a : ambient density ($Kg.m^{-3}$)

ρ_j : jet density ($Kg.m^{-3}$)

ρ_r : reference density ($Kg.m^{-3}$)

υ : fluid kinematic viscosity coefficient ($m^2.s^{-1}$)

Ω : disk rotation rate ($rad.s^{-1}$)

ψ : stream function ($Kg.s^{-1}$)

GENERAL INTRODUCTION

Jet-like helical flows , which result from the coupling and combined action of axial fluid streams and swirl are frequently observed to occur in unbounded environmental geophysical flows (tornadoes, dust-devils, water spouts etc….) as well as in a variety of confined industrial applications (chemical reactors, bioreactors , mixing and combustion devices, hydrocyclones etc….).

It is well established that such swirling flows are controlled by the competition between the strengths of axial and azimuthal motions, and beyond a threshold of their ratio (commonly defined as the swirl number) the jet core undergoes an abrupt flow stagnation and rapid expansion; giving rise to the 'vortex breakdown phenomenon'. Depending on the swirl strength, this vortex pattern may develop into various forms: bubble type with stagnation points, spiral and conical structures etc….

Numerous investigations focused on attempts to develop strategies for controlling the onset conditions and evolution of this fundamental aspect of vortex dynamics. These studies, based upon kinematic, geometric and thermal means, were mainly motivated by the breakdown behavior, which can surprisingly be either beneficial or harmful; depending on the application considered. For instance, breakdown enhances mixing flow properties in chemical reactors, acts as a flame holder in combustion devices which increases combustion efficiency, ensures smooth oxygen transport required for cells growth in bioreactors etc…… By contrast, it was observed to occur over aircraft delta wings where, at high incidence, can cause a sudden drop of the lift and a rapid loss of flight control.

Motivated by the above findings, the current study explores a thermal mean of controlling the stagnation flow conditions and associated breakdown onset which develop within a disk-cylinder system subjected to differential rotation of its end walls. This benchmark geometry is adopted as it provides well defined boundary conditions and the induced vortex flows involve minimum control parameter; thus very amenable to numerical modeling and experimental set ups and operating conditions. Besides, despite its apparent simplicity, the induced vortex flows are very complex.

Thermal buoyancy is induced by a warm/cool uniform axial injection applied upstream the vortex. Prior to this, a bubble type breakdown is first evidenced in the isothermal configuration subjected to neutral (iso-density) as well light/heavy dye injection in order to

numerically simulate recent experimental findings, assess the method of solution and attempt to provide further detailed vortex characteristics difficult to capture by visualization.

The layout in this thesis is as follows: the chapter I introduces the fundamental aspects of helical flows prior to a review of selected past works devoted to the breakdown phenomenon and the various methods of its control. The mathematical formulation which led to the identification of the main physical control parameters is presented in chapter II, while the numerical approach, the commercial code, its implementation and validation are described in chapter III. In Chapter IV, is explored numerically the isothermal configuration which displays on-axis breakdown, subjected to small density variation implemented by axial injection as reported in recent experiments. Chapter V provides results on the sensitivity of the onset conditions and breakdown development to thermal buoyancy, applied by war/cool injection. Finally, concluding remarks summarize the findings and give perspectives for future work.

INTRODUCTION AND LITERATURE SURVEY

I.1. Background

Fluid flows in nature (environment fig. I.1) and in a variety of industrial applications are frequently observed to display localized distorted streams which develop into various forms of vortex patterns [1,2,3]. In this work, interest is mainly focused on the most intriguing vortex phenomenon, commonly referred to as vortex breakdown, whose physical mechanisms are still not fully understood and therefore difficult to predict [4]. Such a fundamental structure, which results from a sudden flow deceleration and stagnation under certain combined kinematic, thermal and boundary conditions, may be either beneficial or harmful and detrimental (thus not desired). This has motivated numerous experimental and numerical investigations, aiming at developing efficient vortex flow control strategies [5,6,7].

To study the various fundamental aspects of the above vortex motion, a large number of configurations may be employed. Although the breakdown phenomenon was first observed to develop over delta wing of an aircraft in aerodynamics (external flow fig I.1) and found to cause rapid loss of control of its maneuverability under high incidence [8], we selected to briefly review the most widely used system involving free jet flows with/without swirl prior to giving a survey which focuses on the benchmark model flows in disk cylinder systems.

Figure I.1: selected vortex illustrations: Environmental vortex (tornado) [AMNH] and vortex in external flows (over an aircraft wings (aerodynamics)) [9]

I.2. Breakdown in Swirling jets

Jets may be defined as fluid streams, generated under pressure, that depart from a nozzle or orifice into a stationary/co-flowing ambient medium. Despite the simple geometry involved, such model flows display very complex vortex patterns which promote and enhance heat and mass transfer efficiency as can be observed in many technical applications; for instance, in cooling systems, combustion chambers, etc… Besides, they are widely explored as benchmark flows which provide detailed fundamental characteristics of turbulence, required to improve the efficiency of numerical modeling in CFD codes. Lucca Negro and Doherty [10] provided an extensive guide to vortex breakdown literature. In figure I.2 are schematically illustrated the main components of a free swirling jet

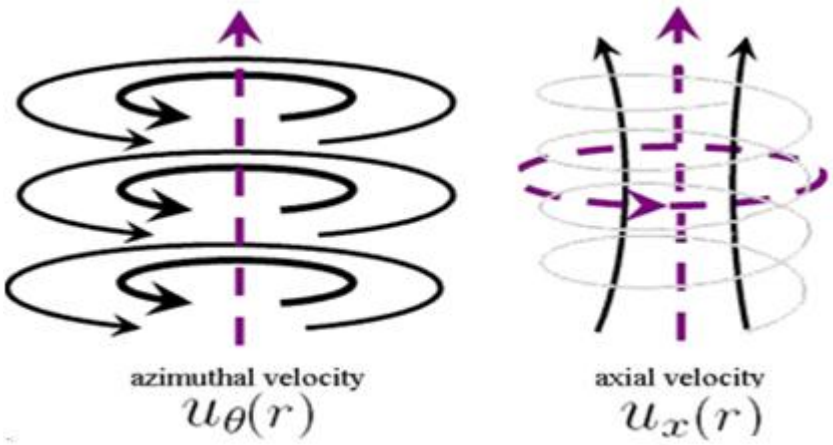

Figure I.2: Schematic of a swirling jet components

I.2.1. Non swirling free jets

Flows in a stream-wise direction with no rotational component can have various forms (round, slotted, oblique etc…) which interact differently with the ambient fluid and hence lead to different flow dynamics and associated momentum and energy transfer behavior as reviewed extensively in the literature [11].

Typically, a **free axisymmetric non-swirling jet** develops an axially diverging shear flow at the interface jet-ambient medium where vorticity is essentially concentrated. Such interface relative motion is very sensitive to the discontinuous jump conditions which apply mainly on the shear stresses; causing the roll up of the

streamlines at the periphery of the axial jet as a result of the well-known Kelvin-Helmhotlz instability. The basic configuration of an axisymmetric non swirling free jet is illustrated schematically in figure I.3.a which indicates a diverging stream with the main regions: a conical potential core formed by the entrainment of the ambient fluid radially inward surrounded by a mixing region formed by the above described mixing shear layer. The length of the potential core is defined by the distance (from the nozzle exit) where the jet mixing region spreads sufficiently inward until it reaches the jet centerline. Beyond this zone, the flow is considered fully developed.

The length of the potential core typically depends on the type of nozzle and exit conditions; typical lengths vary generally over the range 2.5D- 8D (D denotes the nozzle diameter) [11,12]. Beyond the potential core, the mixing region continues to spread as the velocity decays at a rate required for the axial momentum conservation and the mean velocity profile approach the self-similar shape of the fully developed flow illustrated in the above figure.

I.2.2. swirling free jets

When a swirl or rotational velocity component is added upstream the nozzle exit, an axisymmetric free jet takes place (Figure I.3.b). In this model jet, the presence of an azimuthal component generates significant radial and axial pressure gradients, unlike a non-swirling free jet where pressure plays a minor role. As the flow progresses downstream from the nozzle exit, the swirl effect eventually vanishes at about 10D; leading to a flow structure which approaches that of a non-swirling free jet [13]. Therefore the most notable flow features appear in the near-field, where swirl is strongest.

For a small change in the swirl, the flow behavior in the jet near-field and mixing region may change dramatically [15]. When the tangential momentum exceeds a certain threshold (relative to the axial momentum) it is well known that the core flow decelerates and abruptly stagnates to give rise to the breakdown phenomenon. This feature, commonly referred to as vortex breakdown, is considered as a disturbance resulting from the competition between the tangential and axial strengths of the momentum.

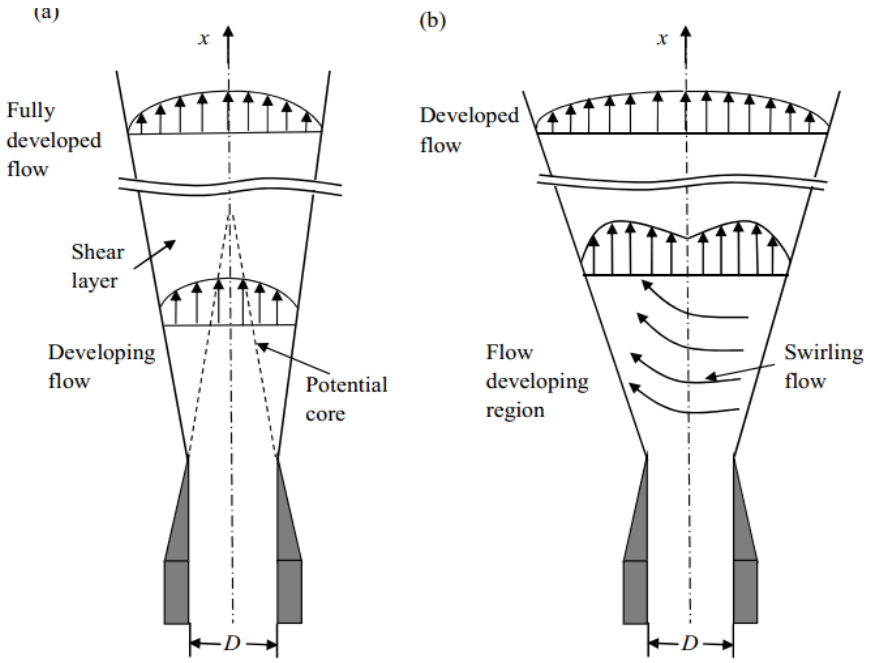

Figure I.3: schematic of the structure of an axisymmetric free jet: (a) non-swirling jet; (b) swirling jet [14]

The corresponding pertinent parameter which describes the behavior breakdown and controls the conditions of its occurrence and development in jets is the swirl number. Various definitions have been used in the related literature, which depend on the configuration adopted [16]. However, the most adequate approach appears that which considers local parameters (within the flow) rather that global ones (which include the geometry etc….) [17].

It is worth noting that such a parameter is difficult to define rigorously in external flows over delta wings (figure I.4); the drawback in this case is the fact that the corresponding tangential and axial momentums are dependent characteristics which interact and correlate and cannot be evaluated or handled separately**.**

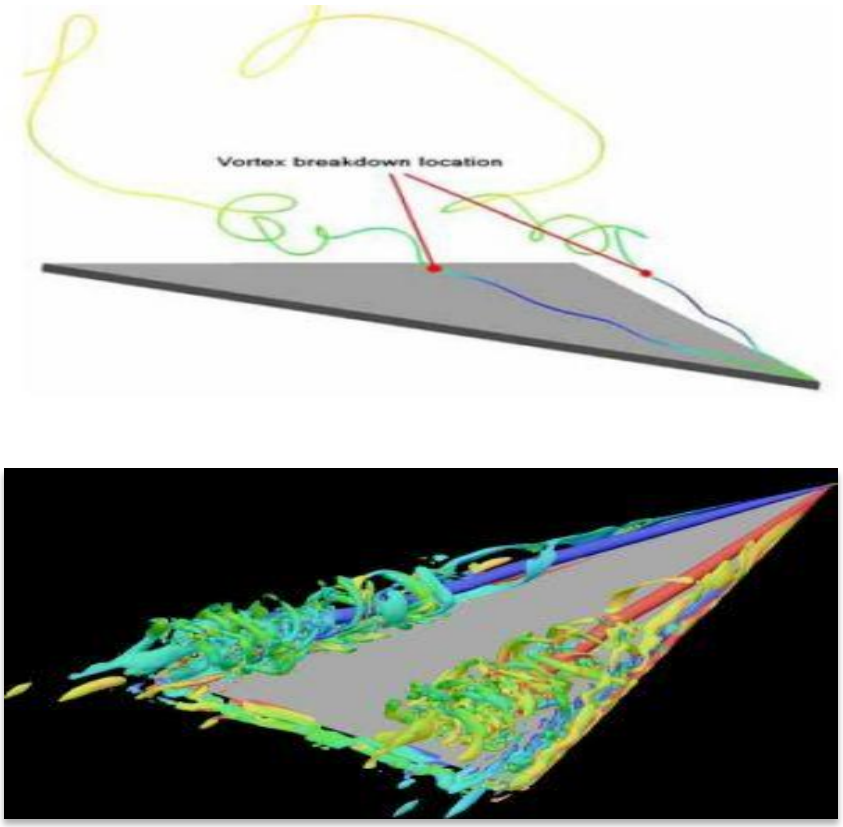

Figure I.4: Primary and secondary vortex flows over a delta wing; (a) schematic model and (b) Direct numerical Simulation [ONERA]

Billant et al (1998) [18] provided updated review of past works devoted to jet flows and characterized experimentally the various breakdown states taking place in a swirling water jet as the swirl ratio S and Reynolds number were varied. The experiments were conducted for two distinct jet diameters by varying the swirl ratio S while maintaining the Reynolds number fixed over the range $300 < Re < 1200$. Breakdown was observed to occur when S reached a well-defined threshold critical swirl number $S_c = 1.3$ which was independent of the Reynolds number and nozzle diameter. Four distinct forms of vortex breakdown were identified: the well documented bubble state, a new cone configuration in which the vortex took the form of an open conical sheet, and two associated asymmetric bubble and asymmetric cone states, which were only observed at large Reynolds numbers. In an intermediate range of Reynolds numbers, the breakdown threshold swirl number displayed hysteresis effect (i.e. vortex breakdown state remain stable even for $S < S_c$ once it had taken

place). The breakdown vortex bubble had been found to remain steady at a fixed station on the jet axis.

Ruith et al (2002) [19] studied numerically vortex breakdown of axisymmetric swirling incompressible flows with jet- and wake-like axial velocity distributions issuing into a semi-infinite domain by means of direct numerical simulations. Low Reynolds numbers were found to yield flow fields lacking breakdown bubbles even for high swirl. In contrast, highly swirling flows at large Reynolds numbers exhibited bubble.

In figure I.5, I.6 are illustrated the various vortex patterns which may occur within a swirling free jet [18,19].

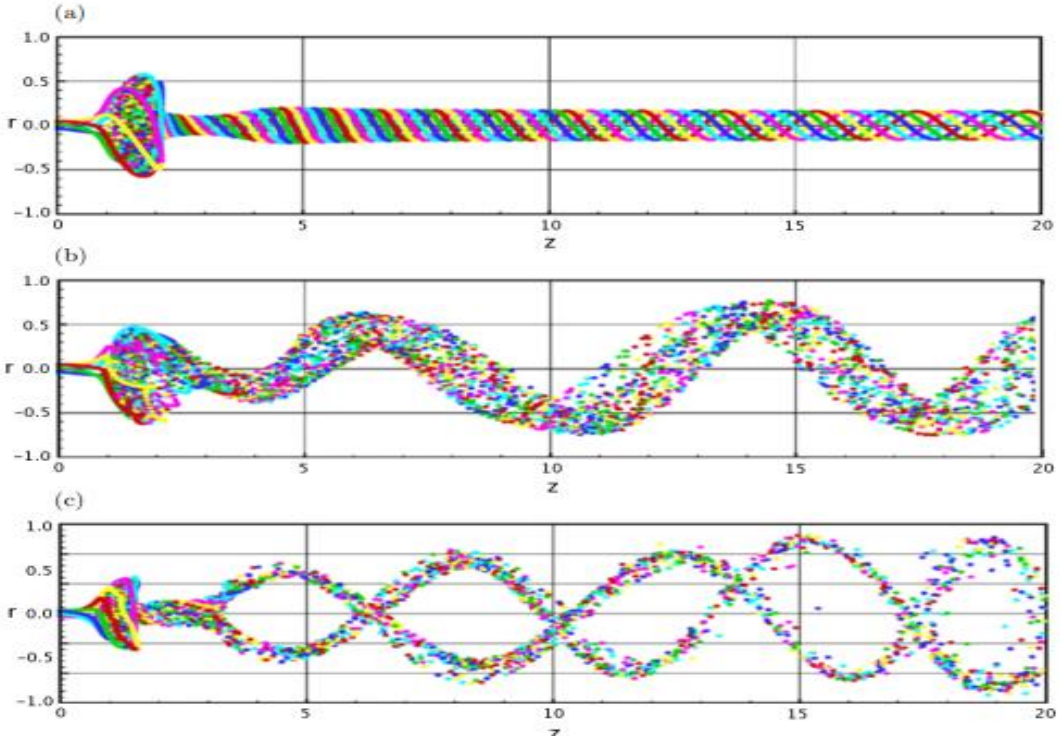

Figure I.5: swirling jet displaying: (a) bubble (b) spiral and (c) double helix breakdown visualized by instantaneous streaklines deduced by direct numerical simulations [19]

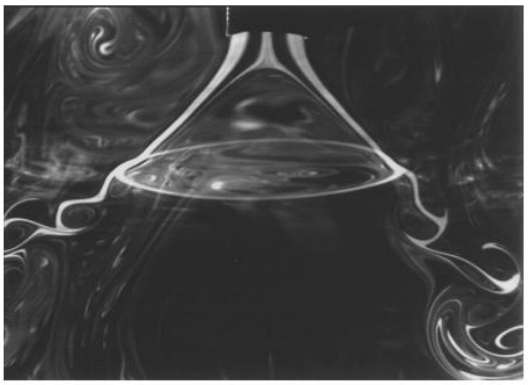

Figure I.6: Flow visualization of an asymmetric cone type of breakdown in a free swirling jet; $Re = 606$ (Reynolds number), $S = 1.37$ (swirl number) [18].

I.2.3. Co-axial swirling jets

An efficient mean to control jet flows characteristics and generate large scale effects, such as jet growth, entrainment and mixing is to consider co-axial jets which consist of an inner axial round jet embedded into an annular co-flowing stream [20]. Both streams may be subjected to differential rotation, in which case two Reynolds numbers and an outer and inner swirl are required to describe the resulting jet flow structures. Such configurations are frequently encountered in industrial applications.

A schematic of two co-flowing jet streams, characterized by different physical properties (density and viscosity) which develop of stagnation point at a distance *h* from the co-axial jet exit [20]

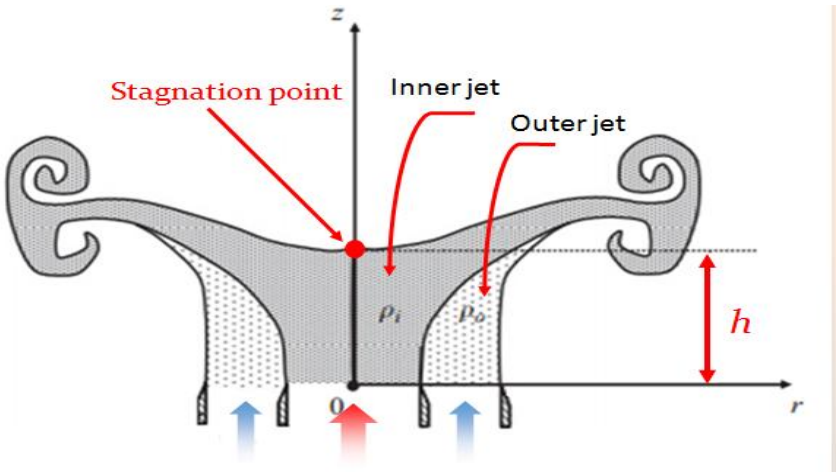

Figure I.7: schematic of the characteristics of two co-flowing streams with variable physical properties. In particular, the co-axial jet stagnation point location [20]

The review articles by Syred (2006) [21] and Huang & Yang (2009)[22] provide an extensive overview of the numerical and experimental evidence for these structures in practical combustion systems. It is reported that swirl dynamics in such systems is still under increasing consideration in order to develop more compact, more efficient and less polluting burners. The outer swirling stream is employed to stabilize the flame through the formation of a central recirculation zone (CRZ) that ensures a supply of fresh reactants to, and removal of hot products away from the flame front. The CRZ is associated to the breakdown phenomenon described above which occurs in swirling flows. For illustration, figure I.8.a represents the scheme of a swirl burner injector in a combustion chamber and figure I.8.b a swirl burner with separate axial fuel injection which discharges into a premixed flame. The recirculation zone is detached from boundaries, which is very advantageous as the flame will not have any negative effect on the walls.

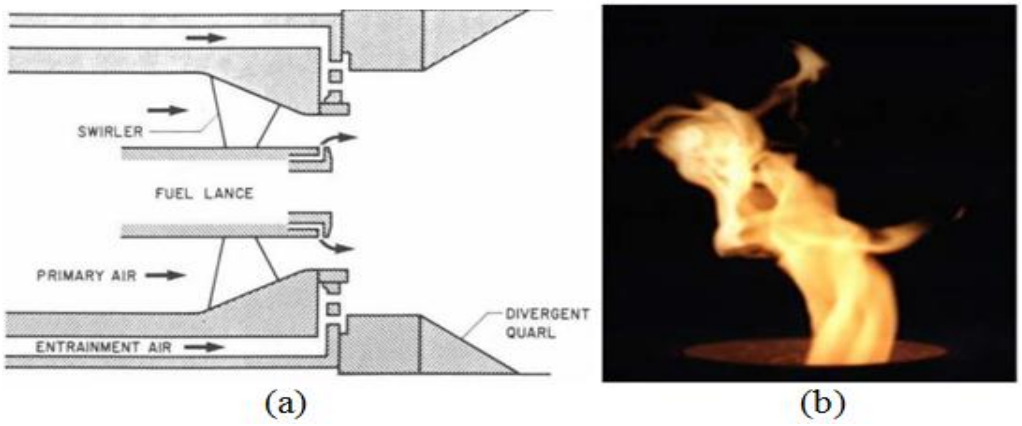

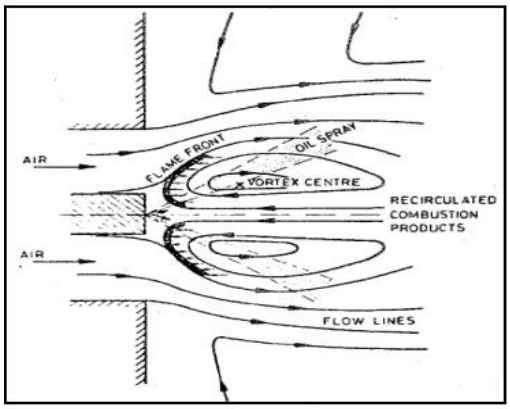

Figure I.8:

(a) Schematic of a swirl burner [23]

(b) Visualization of swirl burner with separate axial fuel injection into a premixed flame [21]

(c) Illustration of a recirculation zone at the exit of the burner (a) [23]

A second application involving co-axial swirling flows is illustrated in figure I.9 which illustrates a device used in pharmaceutical industry as a customized personal ventilation system. This device filters the air to be inhaled, separating it from unwanted particles by means of coaxial jets in differential rotation. The swirling flow exerts a centrifugal force on the particles so that they eventually hit the truncated conical wall, lose momentum and fall down. Clean gas can thus leave the cyclone separator through a central orifice.

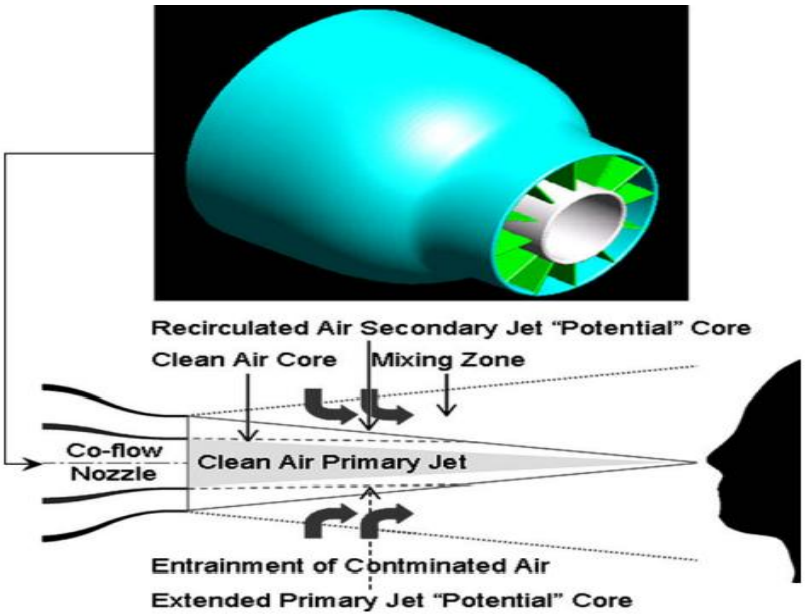

Figure I.9: Mixing co-flow nozzle [24]

I.3. Breakdown in a confined medium

Helical flows which display breakdown may be generated in an enclosed cylindrical cavity whose boundaries may be driven in differential rotation. Unlike the previous configurations, this model flow requires only two main parameters for the description and analysis of its structure and characteristics. Moreover, the boundary conditions are well defined, which renders the configuration more amenable to experimental handling and numerical modeling. Besides, despite the apparent simplicity of this geometry, the induced dynamics may display very complex features and flow regimes, such as the breakdown phenomenon akin to the one evidenced in the case of swirling jets. These arguments have attracted and motivated even numerous investigations, aiming at highlighting the fundamental physical aspects of breakdown.

The helical flow pattern driven by the rotation of a single or two of the end walls of a vertical cylinder may display secondary meridian vortical structures which superimpose to an ambient primary circulation. Among this pattern, the phenomenon of bubble type breakdown may occur along the cavity axis and/or a toroidal type (ring type) vortex. This latter vortex may only appear when both top and bottom walls rotate. In the case of a single end wall rotation, the main parameters which govern the resulting flow dynamics within the enclosed cylinder reduce to: the rotational

Reynolds number $Re = \Omega R^2 / \nu$ and the cavity aspect ratio $\Lambda = H / R$; where R and H are the cylinder radius and height respectively, Ω the end wall uniform angular velocity, and ν the fluid kinematic viscosity (Figure I.10). When both end walls rotate an additional parameter is required to account for the influence of rotation rate ratio and relative direction of rotation; namely, $S = \frac{\Omega_t}{\Omega_b} \left(\lessgtr 0; \Omega_b \neq 0 \right)$, where the indices refer to top and bottom disks.

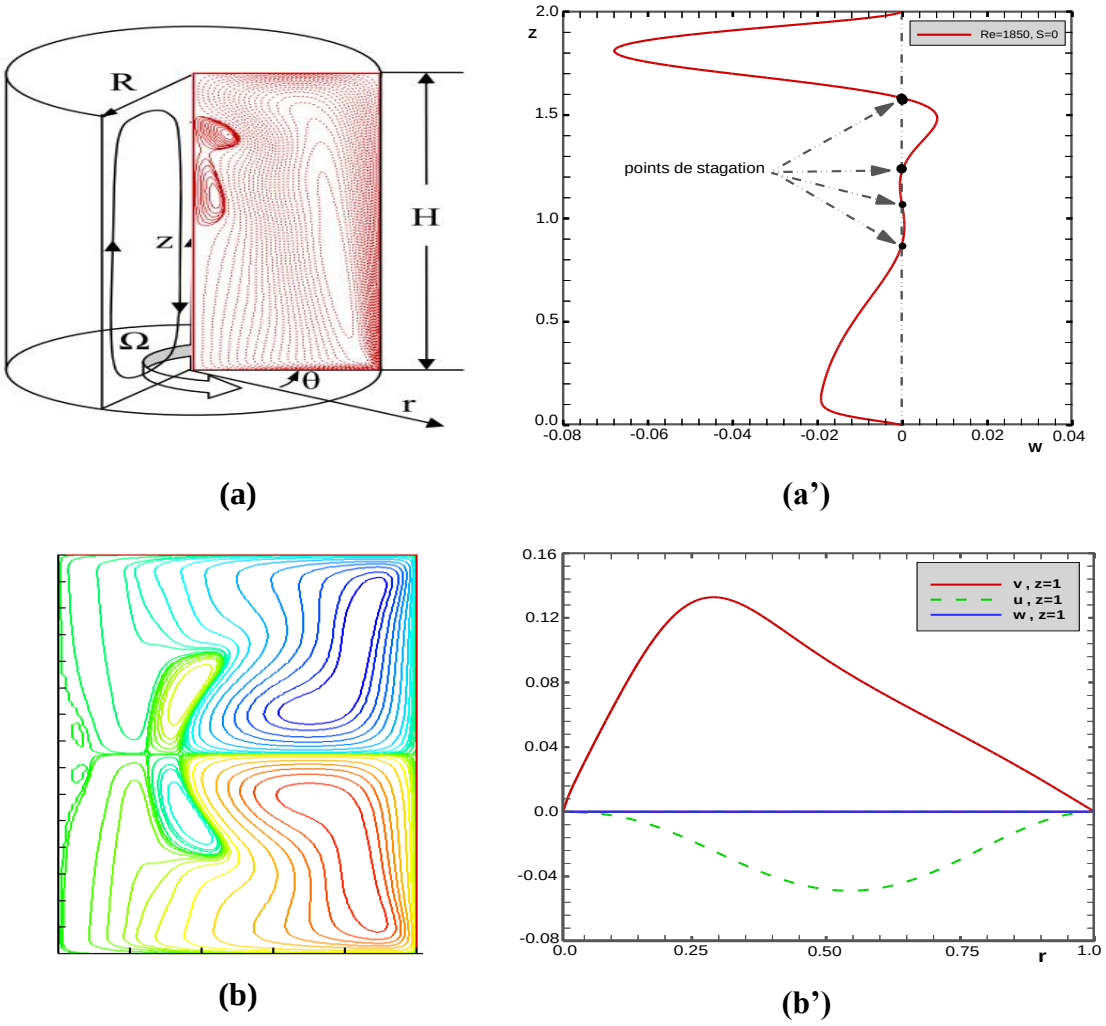

Figure I.10: (a) Sketch of a cylindrical enclosure with rotating bottom disk including the flow direction and the numerical domain which displays a bubble type breakdown **(b)** meridian ring (toroidal) type vortices driven by exact co-rotation of both end disks [25]; **(a')** axial velocity profile **(b')** velocity distribution at mid-depth

The various VB types suggested to occur in a cylinder are sketched in figure I.11 [26] under the variation of the rotation rates of the end disks. The mid-plane symmetries are deduced in the case of exact co-rotation while asymmetries are reported when the walls are subjected to differential rotation.

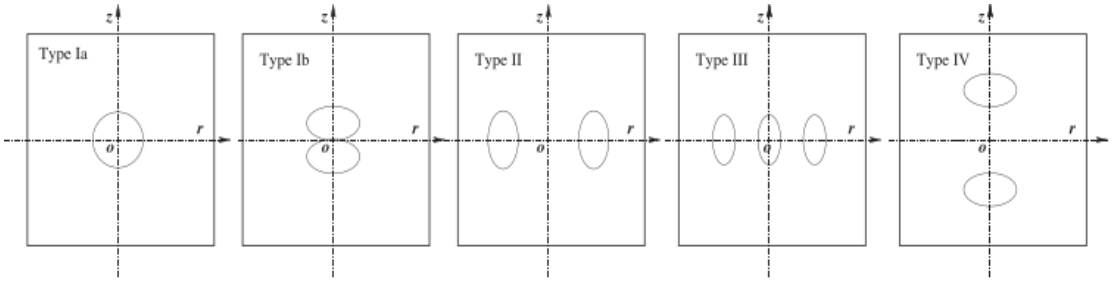

Figure I.11: a sketch of the topological patterns in the meridional plane [26]; Single centered VB, two coalescent VB, two and three ring type mid-plane bubbles (exact co-rotation of both end wall), two on-axis VB.

Figure I.12 shows qualitative typical vortex breakdown structures driven by a single rotating disk of a vertical cylindrical enclose; obtained experimentally by dye injection (from the stationary disk center) and visualized by laser, at $\Lambda = 2.5$ and under the influence of varying Re over the range $1918 \le Re \le 2490$ while Figure 8 illustrates the various flow topologies resulting from the variation of the cavity aspect ratio $(1.495 \le \Lambda_h \le 2.5)$ at fixed Reynolds number $Re = 1900$.

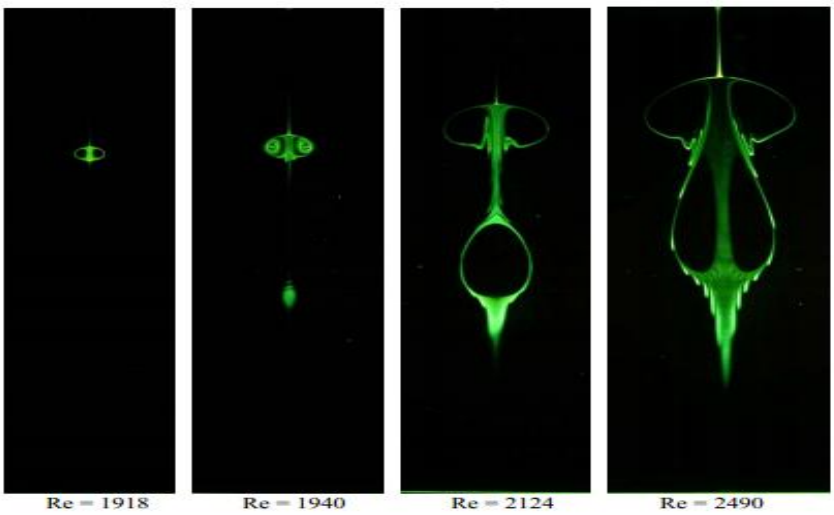

Figure I.12: laser cross-section of vortex breakdown structures at Λ=2.5for different Reynolds numbers. Flow images were captured using florescent dye [27].

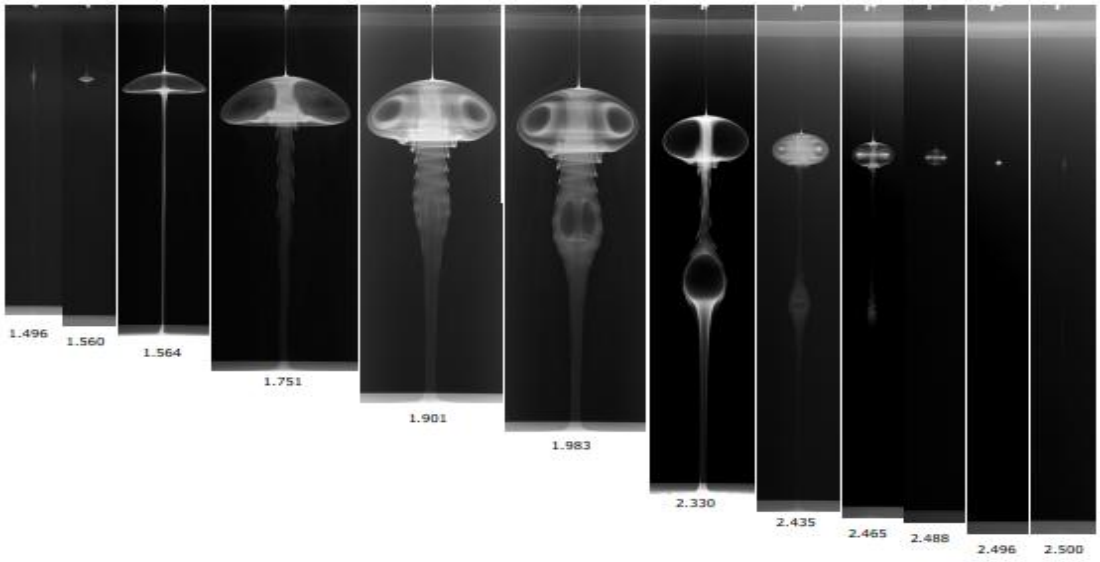

Figure I.13: Vortex breakdown structures at $Re = 1900$ for different aspect ratios. Flow images were captured using food dye [27].

Bubble type breakdown in a cylinder was first visualized and identified experimentally by Vogel [28,29]. A large number of systematic experiments were carried out by Escudier [30], by varying gradually Λ and Re over the approximate ranges $1 < \Lambda < 3.7$ and $1000 < Re < 4000$, which led to the establishment of a detailed benchmark (Re, Λ) stability diagram mapping regions with and without breakdown (up to three bubbles were captured by dye visualization) and the corresponding steady and oscillatory flow regimes. Some more detailed characteristics were later added to the diagram by Iwatsu [31], through numerical simulations. The stability diagram mapping regions of breakdown and flow characteristics, obtained in the configuration based on a single end wall rotation, is depicted in figure I.14 [31].

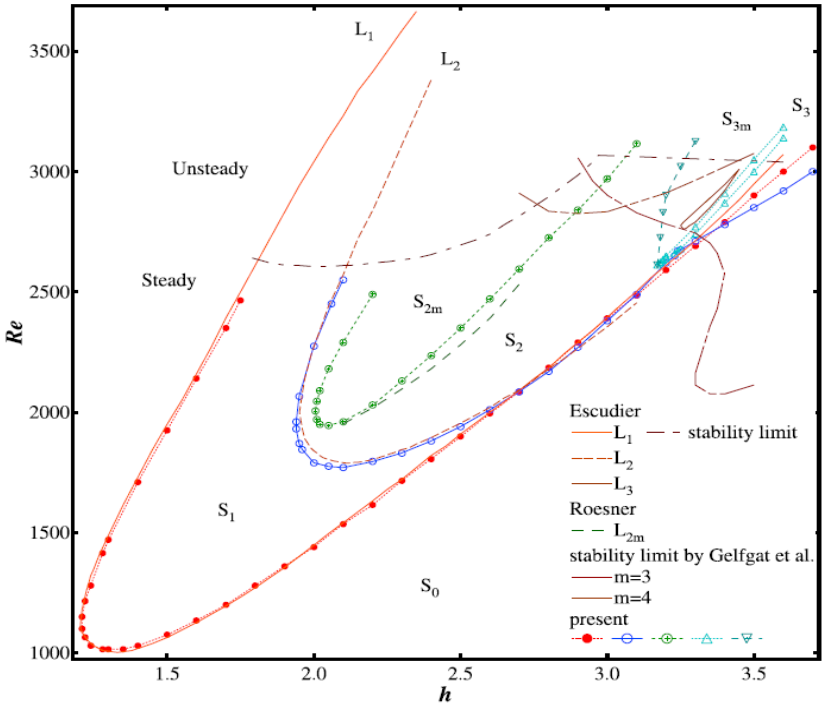

Figure I.14: Regions of breakdown onset and flow regimes: current results under isodensity injection (*distinct* × symbols) added for comparison to detailed stability diagrams supplied by Iwatsu et al. (absence of injection) [31]

As already mentioned above, numerous numerical studies were carried out to model vortex flows in a cylinder, considered as benchmark configuration as the required boundary conditions and geometry are well defined. In particular, since the establishment of Escudier's diagram and also due to the development of numerical tools which, when correctly implemented, allowed to reproduce qualitative experimental conditions and provided in certain cases detailed additional information to complement experimental findings [32,33,34,35].

I.4. Selected studies on vortex flows control

Several prior studies provided means of controlling breakdown onset as it can be harmful / beneficial, depending upon the application considered. Hereafter, are presented selected investigations based on kinematic, geometric and thermal means of vortex flows control.

Of note, Mullin et al. [36] demonstrated the effects of including a tapered centre body and showed it to alter significantly breakdown onset and location. In

particular, they argued that the inhibition / suppression of the vortex structure depended on the axial pressure gradient sign, induced by the conical axial rod, whose circular base is sealed to either the rotating or the stationary disk of the enclosure.

In bioengineering applications, maximum mixing flow control within a bioreactor may be induced smoothly under low shear, by the presence of breakdown which provides a non-intrusive, non-damaging and effective mean of oxygen transport and nutrient required for cell and tissue growth [37,38,39].

Manunga et al. [40], through numerical simulations and dye visualizations, attributed the effective vortex control to the role of vorticity strength, modified upstream of the vortex by the differential rotation of a partial rotating disk flash mounted into the top lid. More recently, breakdown topology in an enclosure shrouded by a polygonal cross section sidewall was explored numerically and experimentally by Naumov et al. [41]. Despite the drastic change in the lateral geometry, the findings revealed that the core flow which displays breakdown remains axisymmetric and the 3D non axisymmetric behavior was remarked in the bulk flow adjacent to the sidewall.

The topology and parameter dependence of breakdown was addressed by Jones et al. [42]. Their analysis led to the identification of the adequate parameters which allowed consistent comparison between bubble breakdown observed in a torsionally driven cylinder flow and the spiral type vortex occurring in flows through open-ended pipes.

More recently, Shtern [43] highlighted the role of the swirl decay as a physical mechanism to control breakdown development.

Thermal effects on confined vortex flows were addressed numerically by, for instance, Lugt et al. [44].Their findings evidenced the sensitivity of breakdown to weak buoyancy caused by an unstable thermal stratification resulting from a slightly heated bottom disk. Under stable thermal stratification, significant effects on the swirling flow topology were reported by Omi et al. [45] who extended the investigation to account for co-/counter-rotating end disks. Compressibility effects were demonstrated by Herrada et al. [46,47], in the case of a non-Boussinesq swirling

flow driven by the bottom disk rotation of a cylinder with and without a central rod. A combination of buoyancy and rod differential rotation provided efficient means of vortex flows control: a forced axial temperature gradient was shown to enhance or eliminate the vortex features; depending on the sign of the temperature gradient.

Flow stagnation and associated breakdown which occur in a swirling jet under effect of thermal buoyancy was addressed by Dina et al. [48] who performed PIV measurements and concluded that a temperature gradient between the jet core and its surrounding fluid affects the breakdown conditions and the form of the vortex pattern as well as its suppression/enhancement; depending on the sign of the gradient. This is illustrated in figure I.15 below which depicts the meridian flow pattern under the combined variation of the rotation rate (rotational Reynolds number) and the temperature gradient (Richardson number).

Prior to these findings, Billant et al [15] reported that vortex breakdown onset and types which occur in a swirling free jet, under a given swirl number, is very sensitive to very small temperature variations in the flow due to non-homogeneous mixing. So, they required that very good care must be taken to ensure uniform mixing to obviate any temperature alterations as confirmed by Dina et al. [48].

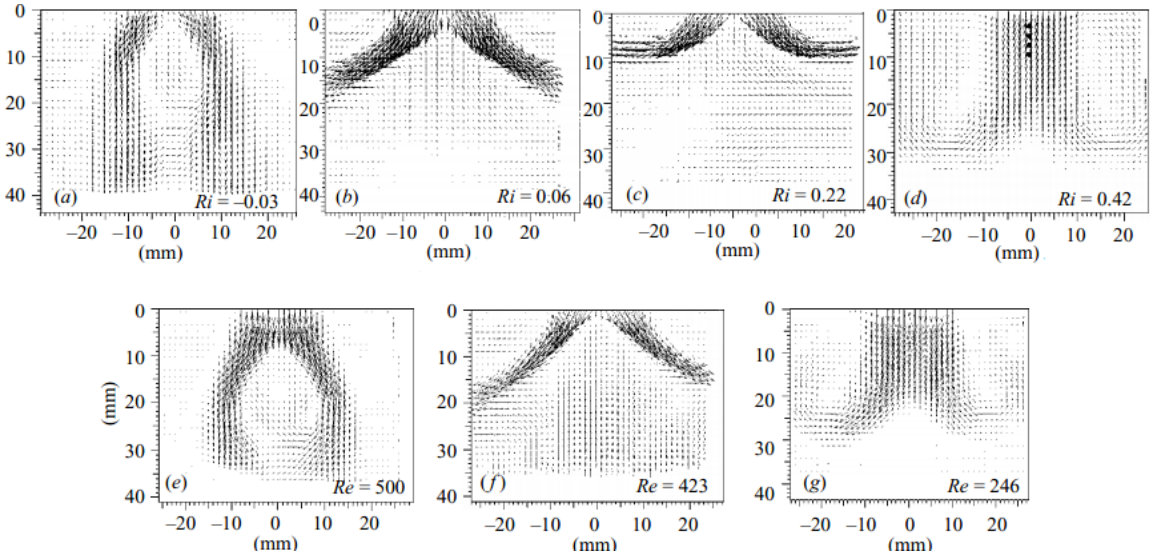

Figure I.15: combined effects of thermal buoyancy (Ri) (Richardson number) and rotational Reynolds number (Re) on the form of breakdown which occurs at the axis of a swirling jet under hot $(Ri<0)$/cold $(Ri>0)$ axial injection, obtained by PIV measurements [48]

In the same context, effects of density variation on a confined isothermal swirling flow which exhibits on-axis vortex breakdown, driven by the top disk rotation of a cylinder, were recently addressed experimentally by Ismadi et al. [49] using axial injection of dye, denser or lighter than the ambient liquid. Flow visualizations indicated that heavy dye enhanced the formation of breakdown while very light dye injection (density variations of order 0.01%) caused the occurrence of off-axis ring type vortices and modified the threshold of breakdown onset. The location of the distinct breakdown types were mapped in a stability diagram established on the basis of varying the density and rotational Reynolds number as illustrated in Figure I.16 below; which maps the distinct breakdown types and corresponding regions of their occurrence.

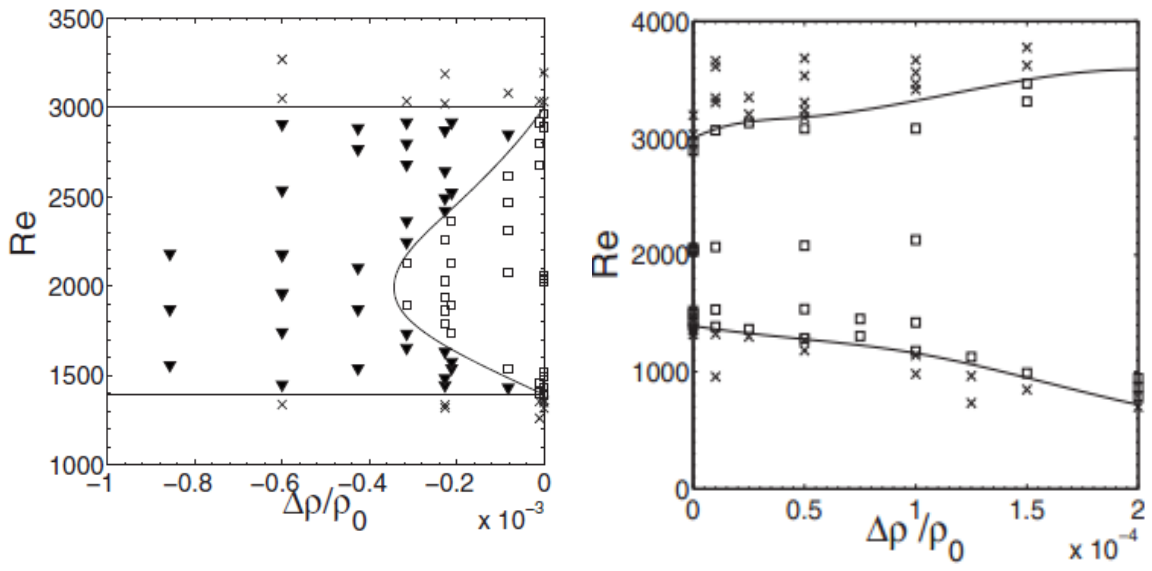

(a) **(b)**

Figure I.16: state diagram mapping regions of ring type (▼) and bubble type breakdown under the variation of *Re* and density ratio [49]: **(a)** configuration under light dye injection, **(b)** configuration under heavy dye injection

Concerns over the symmetry/asymmetry of on-axis breakdown in a cylinder were noted by several investigators: dye visualizations often provide images of vortices with asymmetric folds while 3D numerical counterparts, under well controlled conditions, predict axisymmetric patterns [50,51,52]. This discrepancy is often attributed to the inevitable imperfections of the set up and operating conditions such as a 0.01% misalignment of the cavity axis [51] or a slight tilt $(\approx 2°)$ of one end disk [52].

The impact of small boundaries misalignment in experimental set ups were analyzed by, for instance, Bronz et al. [47] and Meunier et al. [48]. Bronz et al. showed that a slight misalignment of cavity axis allowed the recovery of axial symmetry. In experiments, Meunier et al. [48] conducted experiments (figure I.17) and theoretical studies on the mixing properties in a closed vertical cylindrical cavity with slighty titlted end walls. PIV measurements of the flow driven by the top tilted rotating disk (with and without the tilting of the bottom end disk) were carried out which led to the following main findings on the sensitivity of the flow dynamics to the applied conditions: under a slight tilt of the rotating lid $(\sim 15°)$ it was found that in the absence of breakdown state, the homogenization time decreased drastically by a factor of 10 as a result of the asymmetry; which corresponds to strong convective mixing. However, they reported that in the absence of breakdown, the same tilt of the top lid had very weak effect while a small tilt $(\sim 2°)$ was revealed sufficient to decrease the mixing time by a factor of 10**.** These findings were verified and recovered theoretically by using Melnikov theory**.**

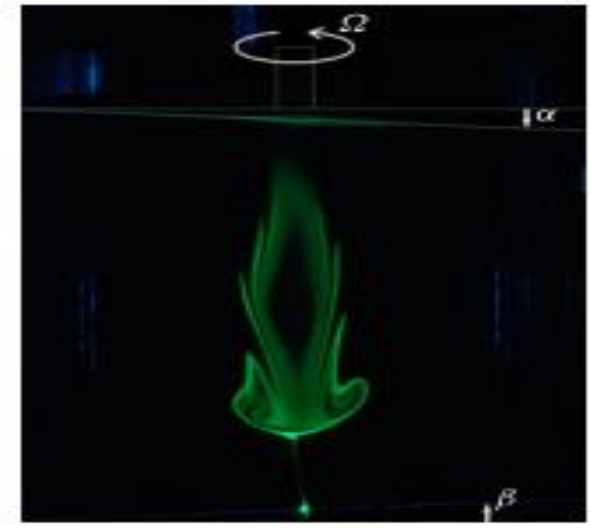

Figure I. 17: dye visualization of the vortex structure obtained by tilting slightly the top rotating disk; $Re = 1000$ and the tilt angle $(\alpha \sim 5°)$ [52]

I.5. Theories and criteria for vortex breakdown

The first theoretical attempts to study the prediction and evolution of the vortex breakdown phenomenon were based on strong assumptions which reduced considerably the physical complexity of the problem and deviated significantly from the real vortex characteristics observed in experiments [53,54]. Due to the advent and development of scientific computing and growth of the numerical tools, additional physical modeling were introduced in the mathematical approaches. An extensive review on the various mathematical approaches devoted to breakdown is given by Shtern et al. [55]

Stuart [56] suggested a classification of breakdown theories which divides them into three categories: breakdown theories based on hydrodynamic instability, theories based on flow deceleration and associated to stagnation points, theories based on the transition from one state to another.

I.5.1. Theories based on hydrodynamic instability

Experimental evidence strongly suggested that vortex breakdown is not a necessary condition for breakdown occurrence. It was observed that hydrodynamic instability appears to be insensitive to downstream boundary conditions which is

contrary to the observations in a vortex breakdown. For instance, application of downstream suction results in a vortex flow without breakdown.

I.5.2. Theories based on deceleration of axial flow leading to stagnation (criterion of Brown and Lopez [4]):

Axial deceleration is in fact a natural tendency of rotating flows that are predominantly axisymmetric. To illustrate this, consider a steady, incompressible and inviscid flow in a nearly cylindrical vortex. The approximate radial momentum equation for pressure P is given by (geostrophic balance): $\frac{dP}{dr} = \frac{v^2}{r}$

Hall [57] suggested that since the angular momentum (circulation) is conserved on a stream surface, the ratio of axial velocity to radial velocity (w/u) upstream of vortex breakdown is positive since $u > 0$ and $w > 0$. In a vortex, the axial pressure gradient is higher than elsewhere; thus, if an adverse pressure gradient is imposed upon the vortex due external flow, say, then its effect on the axis is maximum and the flow naturally tends to decelerate**.** This idea is used by Lopez and Brown [58] who derived a criterion of occurrence of a breakdown bubble in the case of inviscid core flow which states that, a necessary condition for breakdown to occur is that the helix angle for velocity must be larger than the helix angle for vorticity. This suggests that the stream will diverge. Also, the physical mechanism of vortex breakdown rely on the production of negative azimuthal component of vorticity.

I.5.3. Theories based on transition from one flow state to another:

Benjamin's [59] theory of conjugate states is based on the idea of criticality which reflects the ability of a given flow to support waves of infinitesimal amplitude. Benjamin explains vortex breakdown as a finite amplitude transition from a supercritical state of flow to a conjugate *subcritical* state. A flow is said to be supercritical if it is unable to support infinitesimal standing waves, while in a subcritical flow standing waves can occur for a given supercritical state. There exist infinitely many conjugate states, but the selected one in a vortex breakdown is *adjacent* to the given primary supercritical state.

Escudier and Keller [60] introduced a transition theory based upon the idea of two-stage transition, extending Benjamin's theory which considers breakdown as a transition state. Figure I. 18 below illustrates a schematic diagram of the transition stages assumed by Escudier and Keller [60].

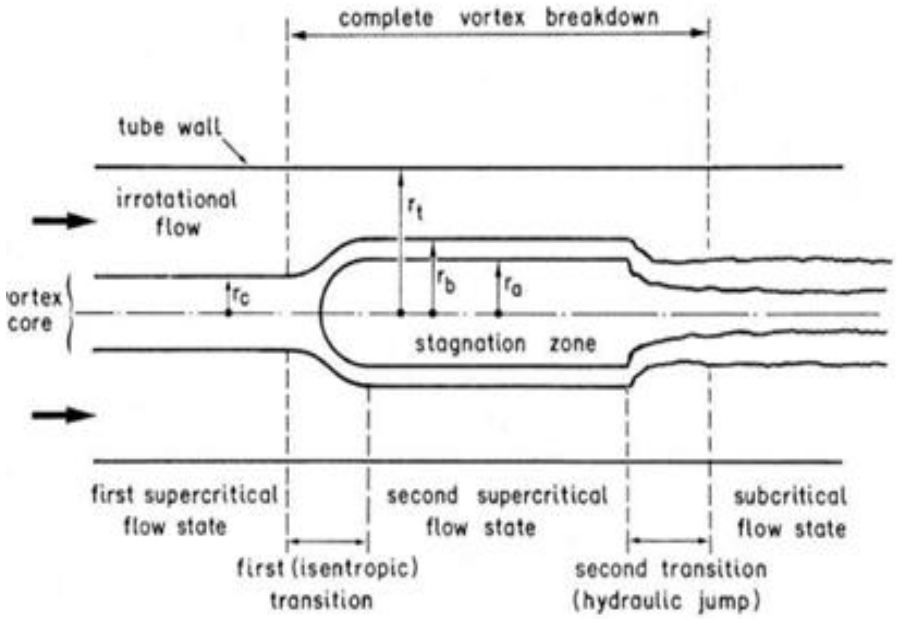

Figure I. 18: schematic of the transition flow states according to the theory of Escudier and Keller [60].

The configuration presented corresponds to that of the flow in a horizontal pipe, which exhibits breakdown. The flow structure upstream breakdown is considered as a vortex core surrounded by an irrotational stream and defined as first supercritical state which undergoes an isentropic transition while the wake flow downstream breakdown is defined as subcritical flow state which is assumed to develop as a result of a hydraulic jump transition. The intermediate region where breakdown occurs is considered as a second supercritical state with nearly stagnated fluid, surrounded by a potential flow. The interface separating the core flow and the ambient irrotational stream is considered as a strong shear layer of rotational flow which is very sensitive to the shear conditions at large Reynolds number. In fact, instabilities develop at the interface causing the roll up of the shear layer and eventually the vortex formation considered as a spiral breakdown compared to the axisymmetric breakdown bubble.

I.6. Conclusion

This chapter was devoted to a review of selected past works carried out on swirling flows, which particularly display the breakdown phenomenon under certain conditions. After a brief introduction on the impact of breakdown in environmental and industrial applications where this physical pattern may occur, particular interest focused on the findings that were achieved on free swirling jets characteristics prior to exploring those attributed to the more controllable configuration which drives vortex flows in disk-cylinder systems. For both selected models, the distinct main parameters were identified and a review of the various available means of controlling the conditions of occurrence and evolution of breakdown were presented and discussed. Finally, recent works on the sensitivity of breakdown characteristics to the experimental conditions, which motivated the present work, are briefly reviewed.

I.7. Chapter references

[1] Leibovich S.. The structure of vortex breakdown. Ann. Rev. Fluid Mech. 10, 221–246, (1978)

[2] Escudier M.P.. Vortex breakdown: Observations and explanations. Prog. Aerosp. Sci. 25 , pp. 189–229, (1988)

[3] Delery J.M.. Aspects of vortex breakdown. Prog. Aerosp. Sci. 30 , 1–59, (1994)

[4] Brown G.L., Lopez J.M.. Axisymmetric vortex breakdown. Part 2: physical mechanisms. J. Fluid Mech. 221, 553-576, (1990)

[5] Liang H., Maxworthy T.. An experimental investigation of swirling jets. J. Fluid Mech. 525. 115–159, (2005)

[6] Mitchell A., Delery J.. Research into vortex breakdown control. Prog. Aerosp. Sci. 37 ,385, (2001)

[7] Jindelt T., Burg J.W., Weide E.T., Hoeijmakers H.W.. Numerical Investigation of Vortex Breakdown. 34th AIAA Applied Aerodynamics Conference, (2016)

[8] Benjamin L., Gilliéron P., Ivani'c T.. Contribution de l'éclatement tourbillonnaire à la réduction de la trainée des véhicules automobiles : approche numérique. C. R. Mécanique 334, 368-372, (2006)

[9] James T Sizemore's photo, Taken on October 26, (2008)

[10] Lucca-Negro O.; O'Doherty T., Vortex breakdown: A review, Prog. Energy Combust. Sci. 27, 431–481, (2001)

[11] Ball C.G., Fellouah H., Pollard A., The flow field in turbulent round free jets. Progress in Aerospace Sciences, 50(0), p. 1-26, (2012)

[12] Ozmen Y., Baydar E., Flow structure and heat transfer characteristics of an unconfined impinging air jet at high jet Reynolds numbers. Heat and Mass Transfer, 44(11), p. 1315-1322, (2008)

[13] Chigier N.A., Chervinsky A., Experimental investigation of swirling vortex motion in jets. Journal of Applied Mechanics, 34(2), p. 443-451. (1967)

[14] Ahmed Z.U. An experimental and numerical study of surface interactions in turbulent swirling jets. https://ro.ecu.edu.au/theses, (1790)

[15] Örlü R., Alfredsson P.H.. An experimental study of the near-field mixing characteristics of a swirling jet, Flow, Turbulence and Combustion, 80(3), p. 323-350. (2008)

[16] Agrawal C. Kumar R., Gupta A., Chatterjee B.. Effect of jet diameter on the maximum surface heat flux during quenching of hot surface. Nuclear Engineering and Design, 265, 727-736, (2013)

[17] Thundil Karuppa Raj R., Ganesan V.. Study on the effect of various parameters on flow development behind vane swirlers. International Journal of Thermal Sciences 47, 1204–1225, (2008)

[18] Billant P., Chomaz J., Huerre P., Experimental study of vortex breakdown in swirling jets, Journal of Fluid Mechanics, 376, p. 183-219, (1998)

[19] Ruith M. R., Meiburg E. Direct numerical simulation of spatially developing, three-dimensional swirling jets. Journal of Turbulence, 3, N65, (2002)

[20] Adzlan A., Gotoda H., Experimental investigation of vortex breakdown in a coaxial swirling jet with a density difference. Chemical Engineering Science 80: 174–181, (2012)

[21] Syred N.. A review of oscillation mechanisms and the role of the precessing vortex core (PVC) in swirl combustion systems. Energy and Combustion Science 32, 93–161, (2006)

[22] Huang Y., Yang V., Dynamics and stability of lean-premixed swirl-stabilized combustion Progress in Energy and Combustion Science 35 293–364, (2009)

[23] Escudier M.P.. Confined vortices in flow machinery, Ann. Rev. Fluid Mech., 19 pp27–52, (1987)

[24] Khalifa H.E., Janos M.I., Dannenhoffer J.F., Experimental investigation of reduced mixing personal ventilation jets» Building and Environment, vol. 44, pp. 1551 –1558, (2009)

[25] Imoula M., Saci R., Benkoussas B., Gatignol R.. Characterization of swirling flows in a partly open cylinder. Journal of Applied Fluid Mechanics (JAFM), Vol. 9, N° 6, 3167-3176, (2016)

[26] Cui X.. A Numerical Study of the Recirculation Zones During Spin-Up and Spin-Down for Confined Rotating Flows. Theoret. Comput. Fluid Dynamics.17, pp. 31–49, (2003)

[27] Cui. Y. Studies of vortex breakdown and its stability in a confined cylindrical container. Thesis submitted for the degree of doctor of philosophy department of mechanical engineering, national university of Singapore, (2008)

[28] Vogel H.U., Experimentelle Ergebnisse über die laminare Strömung in einem zylindrischen Gehäuse mit darin rotierender Scheibe. Max-Planck-Inst. Bericht 6, (1968)

[29] Vogel H.U., Rückströmungsblasen in Drallströmungen. In estschrift zum 50-j ährigen Bestehen des MPI für strömungsforschung, 263-272. Hubert, Göttingen, (1975)

[30] Escudier M.P., Observations of the flow produced in cylindrical container by a rotating endwall. Exp. Fluids 2, 189-196, (1984)

[31] Iwatsu R. Koyama S., A resolution independent solution for confined axisymmetric vortex breakdown flow, J. fluid science and technology, 2, N°1, 215-225, (2007)

[32] Fujimura K., Koyama H.S., Hyun J. M.. Time-dependent vortex breakdown in a cylinder with a rotating lid. ASME J. Fluids Eng. 119, 450, (1997)

[33] Bhattacharyya S. Pal A.. Axisymmetric vortex breakdown in a filled cylinder. Int. J. Eng. Sci. 36, 555, (1998)

[34] Husain H. S., Shtern V., Hussain F.. Control of vortex breakdown by addition of near-axis swirl, Phys. Fluids 15,271, (2003)

[35] Mununga L., Hourigan K., Thompson M.C., Leweke T.. Confined flow vortex breakdown control using a small rotating disk. Phys. Fluids 16, 4750-4753, (2004)

[36] Mullin T., Kobine J.J., Tavener S.J., Cliffe K.A.; On the creation of stagnation points near straight and sloped walls. Physics of Fluids, 12, 425–431, (2000)

[37] Gooch K.J., Kwon J.H., Blunk T., Langer R., Freed L.E., Vunjak-Novakovic G.. Effects of mixing intensity on tissue-engineered cartilage. Biotechnol. Bioeng. 72, 402–407, (2001)

[38] Khalifa H.E., Glauser M.N.. Low-mixing nozzle for personal ventilation. US Provisional Patent Application 60, 826,829, (2006)

[39] Egger D., Fischer M., Clementi A., Ribitsch V., Hansmann J., Kasper C.. Development and Characterization of a Parallelizable Perfusion Bioreactor for 3D Cell Culture. Bioengineering, 4(4), 51, (2017)

[40] Mununga L., Lo Jacono D., Sørensen J.N., Leweke T., Thompson M.C., Hourigan K.. Control of confined vortex breakdown with partial rotating lids. Journal of Fluid Mechanics, 738, 5–33, (2013)

[41] Naumov I.V., Podolskaya I.Y.. Topology of vortex breakdown in closed polygonal containers. Journal of Fluid Mechanics, 820, 263–283, (2017)

[42] Jones M.C., Hourigan K., Thompson M.C.. A study of the geometry and parameter dependence of vortex breakdown. Physics of Fluids, 27, 044102, (2015)

[43] Shtern V.N., Torregrosa M.M., Herrada M.A.. Development of a swirling double counterflow. Physical Review E, 83(5), 056322, (2011)

[44] Lugt, H. J., and Abboud, M. Axisymmetric vortex breakdown with and without temperature effects in a container with a rotating lid. Journal of Fluid Mechanics, 179 (1), 179, (1987)

[45] Omi, Y., Iwatsu, R.. Numerical study of swirling flows in a cylindrical container with co-/counter-rotating end disks under stable temperature difference. International Journal of Heat and Mass Transfer, 48, 4854–4866, (2005)

[46] Herrada, M. A., &Shtern, V. Control of vortex breakdown by temperature gradients. Physics of Fluids, 15, 3468–3477, (2003a)

[47] Herrada, M. A., and Shtern, V. Vortex breakdown control by adding near-axis swirl and temperature gradients. Physical Review E, 68, 041202, (2003b)

[48] Dina M., and Jacob C. The effect of buoyancy on vortex breakdownin a swirling jet. J. Fluid Mech. vol. 571, 177–189, (2007)

[49] Ismadi M.Z.P., Meunier P., Fouras A., Hourigan K.. Experimental control of vortex breakdown by density effects. Physics of Fluids, 23, 034104, (2011)

[50] Jones M.C., Hourigan K., Thompson M.C., Study of the geometry and parameter dependence of vortex breakdown, Physics of Fluids, 27, 044102, (2015)

[51] Brons M., Shen W.Z., Sorensen J.N., Zhu W.J., The influence of imperfections on the flow structure of steady vortex breakdown bubbles, Journal of Fluid Mechanics, 578, 453-466, (2007)

[52] Meunier P., Hourigan K.. Mixing in a vortex breakdown flow. Journal of Fluid Mechanics, 731 195-222, (2013)

[53] Pradeep M., Joseph M.. Bubble and conical forms of vortex breakdown in swirling jets. Journal of Fluid Mechanics 873 , 25. 322-357, (2019)

[54] San To Chan, Jesse T. Ault, Simon J. Haward, E. Meiburg, Amy Q. Shen. Coupling of vortex breakdown and stability in a swirling flow. Phys. Rev. Fluids 4, 084701, (2019)

[55] Shtern V., Hussain F.. Collapse, symmetry breaking, and hysteresis in swirling flows. Annual Review of Fluid Mechanics, 31(1), 537–566, (1999)

[56] Stuart J.T.. A critical review of vortex-breakdown theory. Vortex Control and Breakdown Behaviour, 2nd Intl Colloquium on Vortical Flows, Baden, Switzerland, (April 6-7, 1987)

[57] Hall M.G.. Vortex breakdown. Annual reviews, 8023, (1972)

[58] Lopez J.M., Brown G.L.. Physical mechanisms of axisymmetric vortex breakdown. Australasian Fluid Mechanics Conference, 10th, Melbourne, Australia, Dec. 11-15, (1989)

[59] Benjamin T.B.. Theory of the vortex breakdown phenomena. J. Fluid Mech.14, 593-629, (1962)

[60] Escudier M.P, Keller J.J.. Vortex breakdown: a two-stage transition. AGARD CP no. 342: aerodynamics of vortical type flows in 3D, paper 25, (1983)

MATHEMATICAL FORMULATION

II.1. Introduction

The flows under consideration are driven in closed cavities with independent rotation of the boundaries. Such model flows require initial and boundary conditions associated to the well-known equations of motion; namely, the Navier Stokes equations and the energy equation when temperature is involved. Despite the apparent simplicity of the geometry considered, the vortex flows resulting from the differential rotation of the boundaries are very complex and the corresponding equations of motion are non-linear, which inevitably require a proper and adequate numerical approach in order to approximately solve them and be able to analyze of the vortex dynamics that can be induced.

In what follows, are first presented the geometries and the corresponding physical models as well as the equations of motion in a dimensional form. A non-dimensional formulation is also given which allowed the definition and identification of the different main parameters which control the flow dynamics and thermal associated thermal transfers involved. The initial and boundary conditions are also specified in different forms. Besides, as the flows under consideration are assumed axisymmetric, the velocity field is expressed in terms of a stream-function-vorticity formulation which allowed an adequate description and interpretation of the vortex structure identified by the streamlines.

II.2. Physical model and formulation

We consider a vertical cylinder of height H and radius R , filled with an incompressible viscous Newtonian fluid, whose top end disk is impulsively rotated with a uniform angular velocity Ω as sketched in Figure II.1. the direction of rotation (clockwise/anticlockwise) does not have any influence at this stage. To allow the study of the density or thermal buoyancy effects on the flow pattern induced by the rotating boundaries the set up includes, at the bottom disk center, either a circular orifice of radius ratio $\delta_o = R_o / R$ to allow a uniformly upward axial fluid injection (opposite to the gravity) or a small rod of aspect ratio $\delta_h = R_r / h$ and radius ratio $\delta_r = R_r / R$ (without injection).

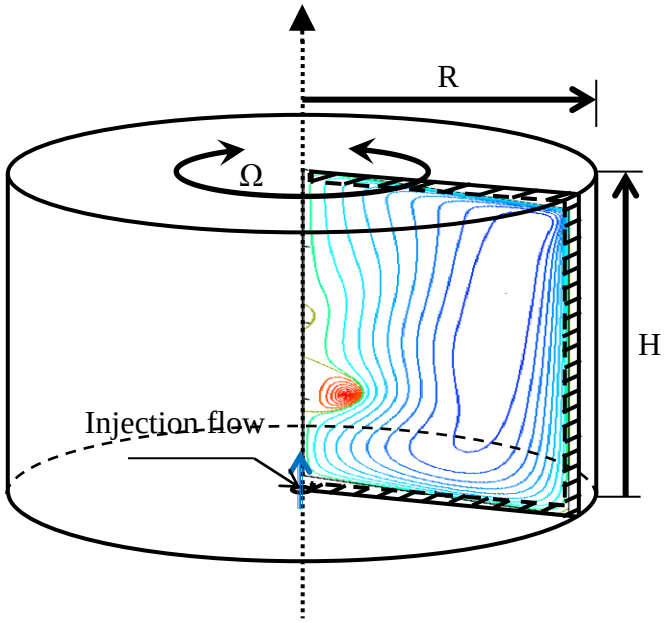

Figure II.1: Schematic of the cylindrical enclosure adopted

Over the range of parameters considered in this work, the flows under consideration are assumed to be laminar and axisymmetric, which start impulsively and evolve in time towards a steady state. So, the numerical domain is reduced to a single meridian plane as illustrated in Figure II.1. Besides, these axisymmetric flows are conveniently described in cylindrical coordinates (r,φ,z) such that the z-axis coincides with the cavity centerline.

II.3. Equations of motion (tensor form)

Using the usual notation, the Navier-Stokes equation in its general tensor form may be expressed as

$$\frac{\partial\left(\rho\vec{V}\right)}{\partial t}+div\left(\rho\vec{V}\otimes\vec{V}\right)=-\vec{\nabla}P+\mu\vec{\nabla}^{2}\vec{V}+\vec{F}_{ext}$$

Where $\vec{V}$ is the fluid velocity, P is the pressure, ρ is the fluid density, μ is the fluid dynamic viscosity and $\vec{F}_{ext}$ is the acceleration due to gravity.

The associated continuity equation can be written in general form as

$$\frac{D\rho}{Dt} + \rho.div\left(\vec{V}\right) = 0$$

II.3.1. Dimensional form of the equations

Due to the geometry adopted, the unsteady Navier-Stokes and energy equations may conveniently be expressed in cylindrical coordinates. Using the axisymmetry condition, the corresponding momentum equations in the radial, azimuthal and axial directions (r,θ,z) may be written respectively in the following form

The radial direction (r-component)

$$\frac{\partial u}{\partial t} + u\frac{\partial u}{\partial r} + w\frac{\partial u}{\partial z} - \frac{v^2}{r} - \beta.(T_0 - T)\frac{v^2}{r} = -\frac{1}{\rho_0}\frac{\partial P}{\partial r} + \nu.\left(\frac{\partial^2 u}{\partial r^2} + \frac{1}{r}\frac{\partial u}{\partial r} - \frac{u}{r^2} + \frac{\partial^2 u}{\partial z^2}\right) \quad \text{(II-1)}$$

The azimuthal direction (θ-component)

$$\frac{\partial v}{\partial t} + u\frac{\partial v}{\partial r} + w\frac{\partial v}{\partial z} + \frac{uv}{r} = \nu.\left(\frac{\partial^2 v}{\partial r^2} + \frac{1}{r}\frac{\partial v}{\partial r} - \frac{v}{r^2} + \frac{\partial^2 v}{\partial z^2}\right) \quad \text{(II-2)}$$

And the axial direction (z-component)

$$\frac{\partial w}{\partial t} + u\frac{\partial w}{\partial r} + w\frac{\partial w}{\partial z} = -\frac{1}{\rho_0}\frac{\partial P}{\partial z} - \beta g\,(T_0 - T) + \nu.\left(\frac{\partial^2 w}{\partial r^2} + \frac{1}{r}\frac{\partial w}{\partial r} + \frac{\partial^2 w}{\partial z^2}\right) \quad \text{(II-3)}$$

The energy equation (neglecting viscous dissipation) reduce to

$$\frac{\partial T}{\partial t} + u\frac{\partial T}{\partial r} + w\frac{\partial T}{\partial z} = \frac{\lambda}{\rho_0 C_P}.\left(\frac{\partial^2 T}{\partial r^2} + \frac{1}{r}\frac{\partial T}{\partial r} + \frac{\partial^2 T}{\partial z^2}\right) \quad \text{(II-4)}$$

Where λ is the thermal conductivity coefficient, C_P the specific heat at constant pressure.

II.3.2. Dimensionless form of the equations and control parameters

It is instructive and advantageous to express the above equations of motion into a non-dimensional form, as this allows the identification of the various main non-dimensional parameters which control the swirling flow dynamics involved.

There are different ways to introduce the reference parameters, in this work we adopt the following definitions to allow comparison with previous findings available in the literature:

-Using $1/\Omega$, R and ρ_r ($\rho_r = \rho_j$ reference density) as time, length and density scales respectively, we define the velocity and pressure references as : $\Omega_b.R$ for the velocity and $\rho_0(\Omega_b.R)^2$ for the pressure reference.

-The temperature scale may be defined with respect to the mean reference temperature $T_0^{'} = \frac{T_a^{'} + T_J}{2}$ such that to obtain the temperature scaling: $T'.\Delta T/(T - T_0')$ where $\Delta T = (T_j - T_0)$

With the above choice of scaling, the non-dimensional velocity, pressure and temperature fields may be written in the form:

$$(u,v,w) = \left(\frac{u'}{\Omega_b.R}, \frac{v'}{\Omega_b.R}, \frac{w'}{\Omega_b.R}\right) \qquad p = \frac{p'}{\rho.\Omega_b^2.\Delta R^2} \qquad T = (T' - T_0')/\Delta T'$$

As the temperature gradients under consideration in the current work are very small, the Boussinesq approximation is assumed to hold, so that the density variation, induced by the temperature gradient $\Delta T = (T_j - T_a)$ set between the injected fluid (or the hot/cold axial small rod) and the ambient one, is accounted for in the buoyancy terms (gravity as well as the centrifugal acceleration) in the following linear form (first order leading term of the Taylor development of the density with respect to temperature) :

$\rho = \rho_r\left(1 - \beta(T - T_r)\right)$ Where β is the thermal expansion coefficient $\left(\beta = \frac{1}{\rho_r}\frac{\partial \rho}{\partial T}\right)$ and ρ_r a reference density corresponding to the reference temperature taken as $T_r = (T_a + T_j)/2$.

We recall that for the rod configuration T_j is simply substituted by the rod temperature T_{rod}.

Under the above assumptions, the non-dimensional equations of motion and the energy equation (neglecting viscous dissipation) may be written in the following form

The continuity equation

$$\frac{u}{r}+\frac{\partial u}{\partial r}+\frac{\partial w}{\partial z}=0 \qquad \text{(II-5)}$$

The radial, tangential and axial momentum equations write respectively,

$$\frac{\partial u}{\partial t}+u\frac{\partial u}{\partial r}+w\frac{\partial u}{\partial z}-\frac{v^2}{r}\left(1-Ri\cdot Fr.T\right)=-\frac{\partial p}{\partial r}+\frac{1}{\mathrm{Re}}.\left(\frac{\partial^2 u}{\partial r^2}+\frac{1}{r}\frac{\partial u}{\partial r}-\frac{u}{r^2}+\frac{\partial^2 u}{\partial z^2}\right) \qquad \text{(II-6)}$$

$$\frac{\partial v}{\partial t}+u\frac{\partial v}{\partial r}+w\frac{\partial v}{\partial z}+\frac{uv}{r}=\frac{1}{\mathrm{Re}}.\left(\frac{\partial^2 v}{\partial r^2}+\frac{1}{r}\frac{\partial v}{\partial r}-\frac{v}{r^2}+\frac{\partial^2 v}{\partial z^2}\right) \qquad \text{(II-7)}$$

$$\frac{\partial w}{\partial t}+u\frac{\partial w}{\partial r}+w\frac{\partial w}{\partial z}=-\frac{\partial p}{\partial z}+Ri.T+\frac{1}{\mathrm{Re}}.\left(\frac{\partial^2 w}{\partial r^2}+\frac{1}{r}\frac{\partial w}{\partial r}+\frac{\partial^2 w}{\partial z^2}\right) \qquad \text{(II-8)}$$

Finally the energy equation reduces to

$$\frac{\partial T}{\partial t}+u\frac{\partial T}{\partial r}+w\frac{\partial T}{\partial z}=\frac{1}{\mathrm{Re.Pr}}.\left(\frac{\partial^2 T}{\partial r^2}+\frac{1}{r}\frac{\partial T}{\partial r}+\frac{\partial^2 T}{\partial z^2}\right) \qquad \text{(II-9)}$$

II.3.3. Control parameters

The above formulation allowed to identify and define the main control parameters required to govern the dynamics of the swirling flows under consideration ; namely, the rotational Reynolds number, the cavity aspect ratio and the Richardson number (which appropriately accounts for thermal buoyancy), defined respectively as:

$$Re=\frac{\Omega R^2}{\nu},\Lambda_h=\frac{H}{R},Ri=\frac{\beta g\,\Delta T}{\Omega^2 R}$$

Here, we recall that $\Delta T=\left(T_j-T_a\right)$ (for the rod configuration T_j is substituted by T_{rod}); ν and β denote the kinematic viscosity and thermal expansion coefficients respectively. Besides, the rod radius ratio δ_r and aspect ratio δ_h , defined above, are kept

constant throughout.

It is noted that the Froude number ($Fr = \frac{\Omega_b^2 (\Delta R)}{g}$ compares the effects/strength of the centrifugal acceleration to the gravitational acceleration) and the Prandtl number ($\mathrm{Pr} = \frac{\mu . C_p}{\lambda}$ fixed here to unity, defines the ratio between the process of thermal and viscous diffusion) are fixed throughout the present calculations.

We recall that, Ω is the rotating velocity of the disc, R is the cylinder disc radius, and υ is the fluid's kinematic viscosity coefficient.

II.3.4. Stream function-vorticity formulation

Besides, as frequently adopted in related swirling flows models, the axisymmetric flows description and analysis are conveniently and naturally done in terms of streamlines, iso-vortices and iso-circulations. In such a case, using the continuity equation and the definition of the circulation, the non-dimensional velocity field (scale: ΩR) may be expressed in terms of the stream function $\psi(r,z)$ (scale: ΩR^3) and circulation $\Gamma = vr$ (scale: $\Omega \mathrm{R}^3$) as follows:

$$(u,v,w) = \left(\frac{1}{r}\frac{\partial \psi}{\partial z}, \frac{\Gamma}{r}, \frac{1}{r}\frac{\partial \psi}{\partial r} \right)$$

This provided a convenient description of the resulting flows in terms of streamlines which indicate local meridian flow directions.

II.3.5. Initial and Boundary conditions

The above non-linear system of Navier-Stokes, continuity and energy equations must be associated to initial and boundary conditions specific to the physical problems introduced above.

The well documented isothermal flow driven by the top disk rotation, in the absence of injection/rod, which displays a steady bubble type breakdown for a given couple of parameters (Re, Λ_h), is defined as a basic state. This model flow is considered as an initial state before injection. Details of the corresponding numerical conditions and flow topology are given in the next chapter.

A. Configuration under injection

- ***Initial conditions***

Let $t<0$ denote the above basic state without injection $\left(U_j=0\right)$, and T_a the corresponding ambient temperature.

At $t=0$, injection is started ($U_j\neq 0, T_j\neq T_a$) and maintained over the time range $0\le t\le t_f$; t_f being dependent on the configuration considered (the lapse of time $t_f\le 300$, which corresponds to a maximum injected fluid volume ratio < 0.05%, was found sufficient to capture the vortex transient behavior over the range of parameters considered).

- ***Boundary conditions which apply for all times*** $\left(0\le t\le t_f\right)$

-No slip and adiabatic conditions are assumed at the rigid walls:

$\left(u,v,w;\partial T/\partial z\right)=\left(0,r,0;0\right)$ Applies at the top rotating lid $\left(z=\Lambda_h, 0\le r<1\right)$

At the stationary sidewall $\left(r=1, 0\le z<\Lambda_h\right)$, $\left(u,v,w;\partial T/\partial r\right)=\left(0,0,0;0\right)$

At the bottom fixed end disk $\left(z=0, \delta_0\le r<1\right)$ we have $\left(u,v,w;\partial T/\partial z\right)=\left(0,0,0;0\right)$

On the centerline $\left(r=0, 0<z<\Lambda_h\right)$, symmetry condition is assumed: $\left(u,v,\partial w/\partial r;\partial T/\partial r\right)=\left(0,0,0;0\right)$

At the inlet orifice $\left(z=0, 0\le r<\delta_0\right)$ axial injection is applied at temperature T_j : $\left(u,v,w;T\right)=\left(0,0,U_j;T_j\right)$.

B. Rod configuration

For the rod case, $t<0$ corresponds to the isothermal basic state with displays a steady breakdown as in the injection configuration. The rod is mounted at the bottom disk center.

$\forall t\ge 0$, no slip condition and constant temperature is applied at the rod surface: $\left(u,v,w;T\right)=\left(0,0,0;T_{rod}\right)$.

The remaining cavity walls are assumed adiabatic and set to the no slip conditions as in the

above injection case

II.4. Conclusion

In this chapter, the geometry (vertical cylindrical enclosure) and physical model under consideration are first introduced. The objective is to model the swirling flows that can be induced by the independent rotation of the boundaries associated to differential heating by means of axial injection or by heating/cooling a small rod. The non-linear system of equations associated to the initial and boundary conditions, required to analyze the vortex flows that may be induced, are given in dimensionless form which allowed the identification of the main dimensionless parameters that govern and control the vortex dynamics.

THE NUMERICAL METHOD OF SOLUTION

III.1. Introduction

The complexity of the physical phenomenon under consideration and the necessity to capture accurately its occurrence and associated main characteristics required a fine and accurate resolution of the non-linear system of the boundary value problem described in detail in the previous chapter.

The approach is inevitably numerical and the method of solution must be chosen on the basis of several conditions which account for the geometry, the flow regime of interest, the range of the control parameters etc….

With the great development of the numerical tools and associated powerful numerical techniques, and as regards to the high cost required to carry out experiments, most investigations in the field of flow dynamics have in recent years been accomplished by means of numerical simulations. This alternative does not supplement experiments but in some particular cases [1], including the present work, when the problem is well defined and the method is correctly implemented, the simulation is able to provide additional information on detailed flow characteristics difficult to capture by the visualization techniques [2,3].

This motivated the present numerical work, in which the resolution is carried out by means of the well-established and most used commercial code ANSYS Fluent (version 15). This latter has been used successfully in previous investigations on complex 3D unsteady flows, involving swirl in various regimes [4,5,6,7] akin to the current work.

We recall that, although the flows under consideration are axisymmetric, the corresponding velocity and vorticity fields are 3D. Besides, the numerical code employs dimensional physical and dynamical properties. However, to allow comparison with previous investigations and for a more general description of the induced flow structures, it appeared instructive and necessary to construct and identify the parameters in dimensionless form as was done in chapter II.

Moreover, the code validation is carefully assessed by first reproducing benchmark configurations available in the literature. In the case of the new contributions, we proceeded by cross-checking certain results obtained by different approaches (when possible).

III.2. Numerical domain

The flow generated by the independent rotation of the boundaries of a vertical cylinder filled with an incompressible Newtonian fluid is conveniently described in cylindrical coordinates (r,φ,z) such that the z-axis coincides with the cavity centerline. As stated in the previous chapter, axisymmetry being assumed over the range of parameters considered, the numerical domain is reduced to a single meridian plane $(r,z)\in]0,1[\times]0,\Lambda_h[$ as illustrated in Figure III.1.

The figure also illustrates meridian streamlines displaying a typical bubble type breakdown which develops at the cavity axis, obtained numerically, along with the main vortex characteristics under interest in this work.

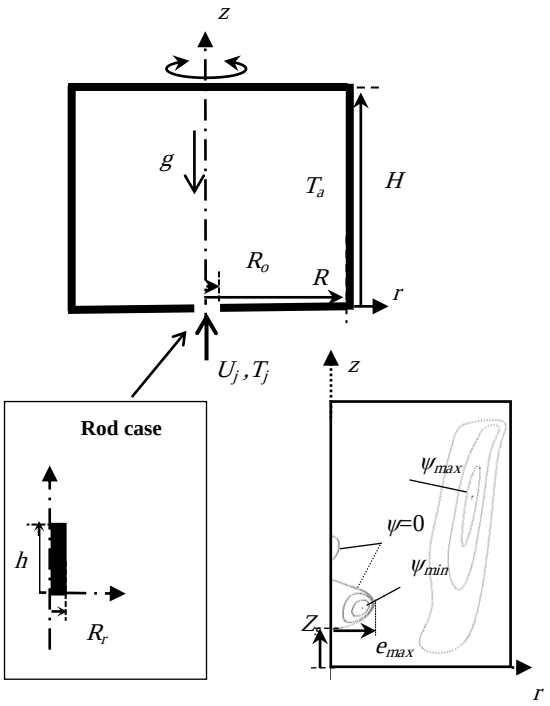

Figure III.1: (Top) Schematic of the geometry and (bottom right) numerical domain which displays a meridian streamline pattern with a typical on-axis two bubble type breakdown and selected vortex characteristics referred to in section 3.1 : Z_s (upstream stagnation point), $e_{\max}$ (bubble radial extent), stagnation line $\psi = 0$, and the maximum volumetric flow rates inside ($\psi_{\min} < 0$) and outside ($\psi_{max} > 0$) the vortex. (Bottom left) the rod configuration.

III.3. Grid generation

To solve the problem under consideration numerically, a grid must be generated in the numerical domain $(r,z) \in]0,1[\times]0,\Lambda_h[$, which constitutes the discrete space for solving approximately the algebraic system of equations issued from the discretization of the continuous problem.

In this work, the generation has been performed by using the software GAMBIT. In particular, an orthogonal grid, especially refined (clustered) in the viscous core region of the helical flow as well as in the vicinity of the boundaries were rapid changes are expected, was utilized in order to adequately capture the requisite details of the vortex characteristics under injection.

The appropriate number of cells and associated time steps which ensure convergence and consistency of the solutions depended on the geometry and the range of parameters considered. So, they were determined on the basis of a grid sensitivity analysis.

Besides, threshold breakdown onset/offset is determined by considering increments of Re of order $\Delta Re = 10$, in the vicinity of the critical values. In addition, to speed up the convergence process and for computational efficiency, simulations were generally initialized with a solution from a lower Re (when available).

-For the selected configuration with $\Lambda_h = 1.98$ which is frequently referred to in this work as this was used in experiments [8], the grid sensitivity of the numerical method was evaluated by considering two sets of non-uniform grids, clustered along the cavity axis with 45000 and 80000 cells, along with a uniform grid of 200×400 elements in the (r,z) plane for comparison.

Time marching was carried out using different time steps over the range $10^{-4} \le \Delta t \le 0.005$. It was found that, a non-uniform grid of 80000 cells associated to a time increment $\Delta t = 0.001$ were relatively sufficient to provide accurately the timewise development of the main vortex characteristics (under warm injection) as well as the corresponding threshold breakdown onset/offset, with a maximum error $< 1\%$ compared to the solution predicted with the smallest time step $\Delta t = 10^{-4}$.

III.4. Numerical procedure

The set of time dependent axisymmetric Navier-Stokes equations together with the mass conservation and energy equation, subjected to the initial and boundary conditions detailed in chapter II, were integrated under the Boussinesq approximation using a finite volume approach, implemented in the well-established CFD package ANSYS Fluent 15 described briefly above.

The laminar solver is adopted and associated to volume of fluid method when injection is applied. This commercial code was recently employed successfully to accurately model various confined as well as jet like swirling flows, which display breakdown, analogous to the configuration under consideration [9,10,11].

We used a segregated solver in which a second order upwind scheme was employed to discretize the convective terms, a first order implicit scheme was adopted for time marching while central differencing is utilized to approximate the diffusion terms. Such a choice was guided by previous numerical experiments [12] which reported successful convergent results with minimum cost.

Pressure-velocity coupling was achieved by using the semi implicit pressure linked equation coupling (SIMPLEC) algorithm. It is worth noting that the pressure-implicit with splitting operator (PISO) algorithm, which is a non-iterative time marching procedure, was also employed but no major advantage was achieved in the current work in terms of computational time.

At the boundaries, Body Force Weighted Scheme is applied and double precision was considered in all calculations.

The Convergence criteria, at each time step, were based upon the asymptotic level reached by the scaled residuals of each equation as well as that of the velocity field.

Overall, the scaled residuals were found to lie between 10^{-10} for the continuity and momentum equations and 10^{-15} for the swirl and energy equations.

III.5. Data Processing

The numerical data have been processed with the powerful software Tecplot. This latter provided very accurate mappings of streamlines contours which are necessary to track the local flow direction, associated to the velocity and pressure distributions. The software also offered various mathematical interpolations to cover the regions lacking data.

III.6. Validation

The accuracy of the simulations was first assessed by simulating the benchmark helical flow, driven by a single disk rotation of a vertical cylinder, in the absence of injection, investigated experimentally by, for instance, Escudier [13] and Iwatsu et al. [14] and supported quantitatively by numerous numerical predictions; for instance, Lopez [15], Iwatsu et al. [14] and Escudier et al. [11].

Further validation is performed in chapters three (III) and four (IV) devoted to the isothermal configuration which includes heavy/light dye injection, explored experimentally by Ismadi et al. [8].

In addition, for the new configurations under thermal buoyancy effects, some sets of results, obtained by solving the unsteady equations for large times, were compared to their counterparts reached by means of solving the steady equations.

III.6.1. Validation in the case of a configuration without injection

In chapter III, it will be shown that for the selected parameters $(Re, Ri, \Lambda_h) = (1850, 0, 2)$, the flow structure generated by a single disk uniform rotation of a vertical cylinder consists of an ambient primary large meridian circulation with two distinct bubble type vortices located along the cavity axis as illustrated in the figures III.2.

The current numerical predictions of the vortex characteristics corresponding to this benchmark flow are found to reproduce accurately those supplied by experiments in the literature [13,14,15]. Indeed, in table III.1 are reported three selected vortex flows characteristics (sketched in Figure III.1); namely, the upstream (first) stagnation point location (Z_s), the radial extent of the vortex pattern $(e_{\max})$ scaled with the cylinder radius, as well as the vortex strengths $\psi_{\min}$ and ψ_{max} (meridian volume flow rates respectively within and outside the vortex structure).

It is remarked that the maximum error estimate is within 0.5% on the stagnation point's location (sensitive criterion for onset /suppression of breakdown) and approximately 1% for the above volume flow rates which is considered as negligibly small.

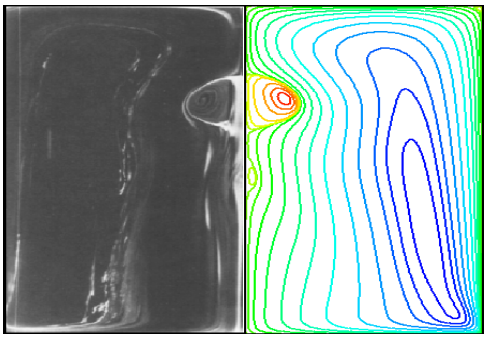

Figure III.2: Flow structure driven by the rotating bottom disk: Re = 1850 experiments by Escudier (image at the left) [13] compared to the present numerical predictions (streamlines)

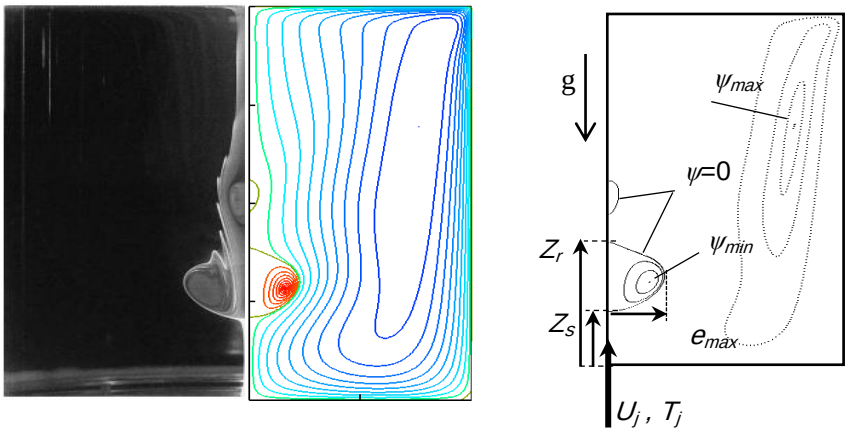

Figure III.3: Flow structure driven by the top rotating disk (Re=1850 Iwatsu [14]) which captures better the second bubble ; the right figure is sketch of the corresponding vortex characteristics

Table III.1.: Values of the flow characteristics: Z_s , $e_{\max}$, $\psi_{\min}$ and ψ_{max} obtained in this work and those provided by experiments [13] and numerical simulations [14]; $(Re, Ri, \Lambda_h) = (1850, 0, 2)$.

Vortex characteristics	Exp. Escudier (1984)	Num. Iwatsu et al. (2007)	Present Work	Error Estimate
Z_s	0.42	0.4231	0.4210	< 0.5%
$e_{\max}$	0.236	0.225	0.2264	<1.56
$\psi_{\min}(10^{-4})$	-	-0.5916	-0.5981	1%
$\psi_{max}(10^{-2})$	-	0.7832	0.7867	< 0.5%

III.7. Conclusion

In this chapter, the numerical approach is presented which consists of a numerical simulation by means of the commercial code ANSIS Fluent15. After a brief introduction and motivation, the grid generation and the method of solution, based on the finite volume method associated to the volume of fluid method, are specified. Finally, the code validation is carried out by reproducing qualitatively and quantitatively the swirling flow patterns and vortex characteristics provided by recent experiments related to the current work.

III.8. Chapter references

[1] Husain H.S., Shtern V., Hussain F.. Control of vortex breakdown by addition of near-axis swirl, Physics of Fluids 15 271-279, (2003)

[2] Brons M., Shen W.Z., Sorensen J.N., Zhu W.J.. The influence of imperfections on the flow structure of steady vortex breakdown bubbles, Journal of Fluid Mechanics, 578, 453-466,(2007)

[3] Meunier P., Hourigan K.. Mixing in a vortex breakdown flow, Journal of Fluid Mechanics, 731, 195-222, (2013)

[4] Sørensen J.N., Gelfgat A.Y., Naumov I.V., Mikkelsen R.. Experimental and numerical results on the three-dimensional instabilities in a rotating disk-tall cylinder flow.Phys. Fluids21, 054102, (2009)

[5] Lopez J. M.. Three-dimensional swirling flows in a tall cylinder driven by a rotating endwall. Phys. Fluids24, 014101, (2012)

[6] Naumov I.V., Dvoynishnikov S.V., Kabardin I.K., Tsoy M.A.. Vortex breakdown in closed containers with polygonal cross sectionl. Phys. Fluids27, 124103, (2015)

[7] Naumov I.V., Podolskaya I.Y.. Topology of vortex breakdown in closed polygonal containers, Journal of Fluid Mechanics, 820, 263–283, (2017)

[8] Ismadi M.Z., Meunier P., Fouras A., Hourigan K., Experimental control of vortex breakdown by density effects, Physics of Fluids, 23**,** 034104 **(**2011)

[9] Marugán-Cruz C., Rodríguez-Rodríguez J., Martínez-Bazán C.. Formation regimes of vortex rings in negatively buoyant starting jets, Journal of Fluid Mechanics 716: 470–486, (2013)

[10] Dennis D.J.C., Seraudie C., Poole R.J.. Controlling vortex breakdown in swirling pipe flows: Experiments and simulations, Physics of Fluids 26 (5): 053602, (2014)

[11] Escudier M.P., O'Leary J., Poole R.J.. Flow produced in a conical container by a rotating endwall, Journal of Heat and Fluid Flow 28: 1418–142, (2007)

[12] Vandoormaaland J.P., Raithby G.D.. Enhancements of the SIMPLE Method for Predicting Incompressible Fluid Flows, Numer. Heat Transfer, Vol. 7, pp. 147163, (1984)

[13] Escudier M.P.. Observations of the flow produced in a cylindrical container by a rotating end wall, Exp. Fluids **2,** 189-196, (1984)

[14] Iwatsu R., Koyama S.A.. A resolution independent solution for confined axisymmetric vortex breakdown flow, Journal of fluid science and technology, 2, 215-225, (2007)

[15] Lopez J.M.. Axisymmetric vortex breakdown, Part 1,Confined swirling flow, Journal of Fluid Mechanics 221, 533-552, (1990)

SENSITIVITY OF ISOTHERMAL SWIRLING FLOWS TO DENSITY VARIATIONS

IV.1. Introduction

The work in this chapter is numerical and concerns the control of the stagnation flow conditions and associated reverse circulations that occur within the core region of a helical confined jet. The control is carried out by means of an axial injection of a fluid slightly lighter/heavier than the ambient fluid. The primary swirling flow is driven by the top disk uniform rotation of a vertical cylinder and the induced secondary vortex structure occurs within its core as an on-axis bubble type breakdown. Besides, the injection is applied upstream of this latter structure from the fixed bottom disk center of the vertical cavity. The main objective of this study is an attempt to first reproduce and then extend numerically, under the same conditions, recent fundamental experimental findings obtained by means of dye injection [1,2,3,4,5]. To the author's knowledge, this numerical contribution does not appear to have been considered in the literature.

IV.2. Basic isothermal flow without injection

We consider a vertical cylinder of height H and radius R, filled with an incompressible viscous Newtonian fluid, whose top end disk rotates with uniform angular velocity Ω as sketched in Figure IV.2 the set up includes, at the bottom disk center circular orifice of radius ratio $\delta_o = R_o / R$ to allow uniform axial fluid injection.

The flow is conveniently described in cylindrical coordinates (r, φ, z) such that the z-axis coincides with the cavity centerline. In accord with the literature [6,7], the induced flow structure under consideration is assumed to be laminar and axisymmetric, within the parameters ranges considered, which led to reduce the numerical domain to a single meridian plane.

The model swirling flows under consideration may sufficiently be described by two main parameters; namely, the rotational Reynolds number Re and the aspect ratio of the cavity Λ_h. Although the investigation was carried out successfully for various aspect ratios and Reynolds numbers, respectively over the ranges: $0.8 \le \Lambda_h \le 2.5$, $250 \le Re \le 2600$, we focused in this subsection mainly on the configuration $(Re, \Lambda_h) = (1850, 2)$; selected for the sake of comparison with previous experiments and numerical simulations.

In the absence of injection, qualitatively, for given low rates of top disk rotation and under effects of boundaries confinement, a clockwise large meridian circulation takes place which superimposes to the initial primary rotational motion. In particular, fluid spirals outward (inward) in the vicinity of the top rotating disk (stationary bottom disk) with the formation of a thin boundary layer on each disk. Along the cylindrical sidewall, flow swirls downward while the bulk helical core is directed axially upward by the Ekman suction effect. Depending on the aspect ratio Λ_h $(\Lambda_h > 1.2)$, as the disk rotation rate increases, it is well established that the flow stagnates at the cavity axis and an adverse pressure gradient takes place; giving rise to one, two or three reverse flow regions commonly referred to as bubble type vortex breakdown.

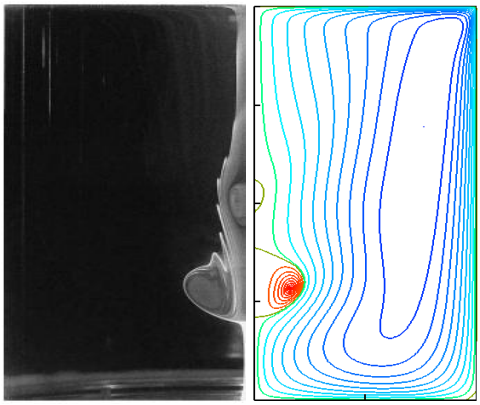

Figure IV.1: Contour plots of meridian streamlines (right) compared with experimental visualization [8]; $Re = 1850$, $\Lambda_h = 2$, iso-thermal and iso-density configuration without injection. Contour values are $\psi = \psi_{max}\,(i/10)^3, \psi_{min}\,(i/10)^3$, $i = 1....10$

In the current work, for the selected parameters $(Re, \Lambda_h) = (1850, 2)$, the onset and location of two distinct axisymmetric bubbles is evidenced numerically and viewed qualitatively in Figure IV.1 by the meridian streamlines. For comparison, alongside this figure is given the corresponding flow topology supplied by visualized dye experiments [8]; showing a good qualitative agreement. The corresponding axial velocity distribution along the cavity axis, supplied only numerically, is depicted in Figure IV.4 which accurately the axial location of the upstream and downstream stagnation points bounding the distinct bubbles, and indicates a change of axial flow direction in the vortex structure. Within this latter, meridian motion is anticlockwise and of weak intensity compared to the ambient clockwise primary circulation

(order of magnitude of the axial velocity inside and outside the bubbles). The direction of the meridian motion within and outside the bubbles is independent on that of the top disk rotation.

Besides, this configuration was found to reproduce very accurately the numerical predictions [8] of various vortex characteristics. Indeed, in Table IV.1 are reported three selected vortex flows characteristics (figure IV.2); namely, the upstream (first) stagnation point location (Z_s), the radial extent of the vortex pattern $(e_{\max})$ scaled with the cylinder radius, as well as the vortex strengths $\psi_{\min}$ and ψ_{max} (meridian volume flow rates respectively within and outside the vortex structure).

It can be remarked that the maximum error estimate is within 0.5% on the stagnation point's location (sensitive criterion for onset /suppression of breakdown) and approximately 1% for the above volume flow rates which is considered as negligibly small.

Table IV.1 Values of the flow characteristics Z_s, $e_{\max}$, $\psi_{\min}$ and ψ_{max} obtained in this work and those provided by experiments [9] and numerical simulations [8]; $(Re, \Lambda_h) = (1850, 2)$.

Vortex characteristics	**Exp. Escudier (1984)**	**Num. Iwatsu et al. (2007)**	**Present Work**	**Error Estimate**
Z_s	0.42	0.4231	0.4210	< 0.5%
$e_{\max}$	0.236	0.225	0.2264	<1.56
$\psi_{\min}(10^{-4})$	-	-0.5916	-0.5981	1%
$\psi_{max}(10^{-2})$	-	0.7832	0.7867	< 0.5%

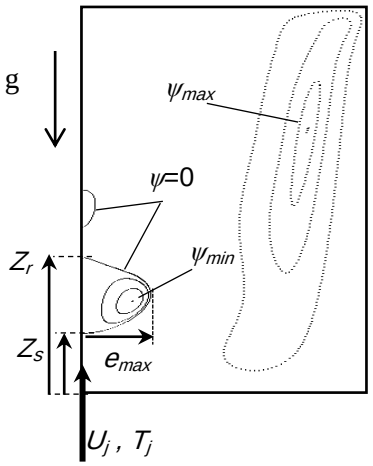

Figure IV.2: Schematic of the numerical meridian plane illustrating two on-axis bubble type breakdown and the corresponding selected vortex characteristics

IV.3. The configuration with neutral injection (iso-density case)

Prior to exploring effects of density variations, it appeared necessary to assess the sensitivity of the vortex pattern to the chosen inlet geometry and associated injection conditions of a fluid characterized by the same thermo-physical properties. For this, we consider the isothermal configuration with an inlet orifice located at the bottom disk center which allows a uniform fluid injection, in the direction opposite to gravity.

For the sake of comparison with experiments [3,4], a uniform injection velocity $U_j = 1.7\times10^{-3} m/s$ is applied at the orifice (radius ratio $\delta_o = R_o/R = 7.69\times10^{-3}$) of two selected distinct basic configurations $(\Lambda_h, Re) = (1.98, 1700)$ and $(\Lambda_h, Re) = (1.98, 2060)$: in the absence of injection, the former displays a single steady and axisymmetric on-axis reverse flow region while the latter undergoes two breakdown bubbles [8] (as in the case discussed in the above section).

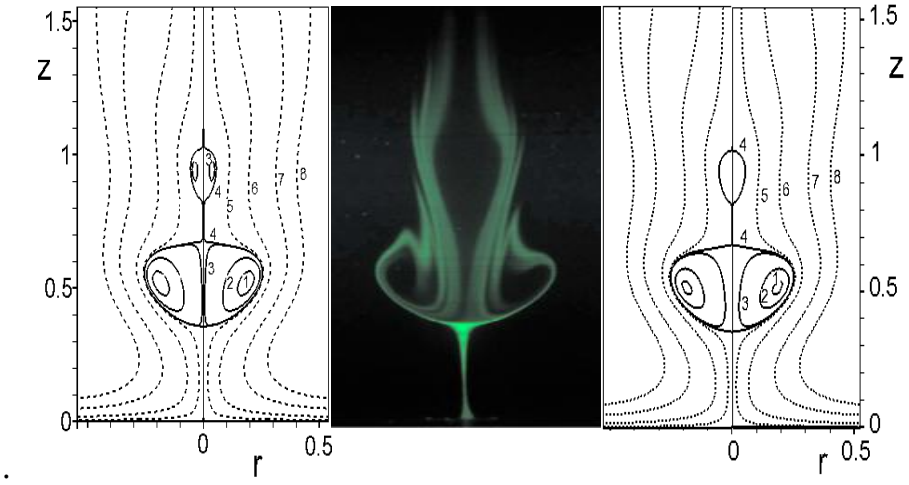

(a) **(b)** **(c)**

Figure IV.3: Close up of the vicinity of breakdown under isodensity injection $(0.5 < r < 0.5, 0 < z < 1.5)$; (a) before injection (b) experiments [3] (under injection) (c) after injection $Re = 2060$

The present calculations for this model flows, revealed minor local effects limited to the vicinity of the inlet orifice. It is found that the injected iso-density fluid is advected axially upward and spirals over the bubble without altering neither its form and size nor the axial location of the two stagnation points bounding the structure, in agreement with experimental

observations [3]. This is evidenced, qualitatively, by comparing the steady flow topologies obtained with and without injection illustrated by the close up region of the vortex structure supplied in figure IV.3 for the selected case (chosen for the sake of brevity) $(\Lambda_h, Re) = (1.98, 2060)$

The above result is confirmed quantitatively by the corresponding axial velocity distribution supplied only by the present calculations.

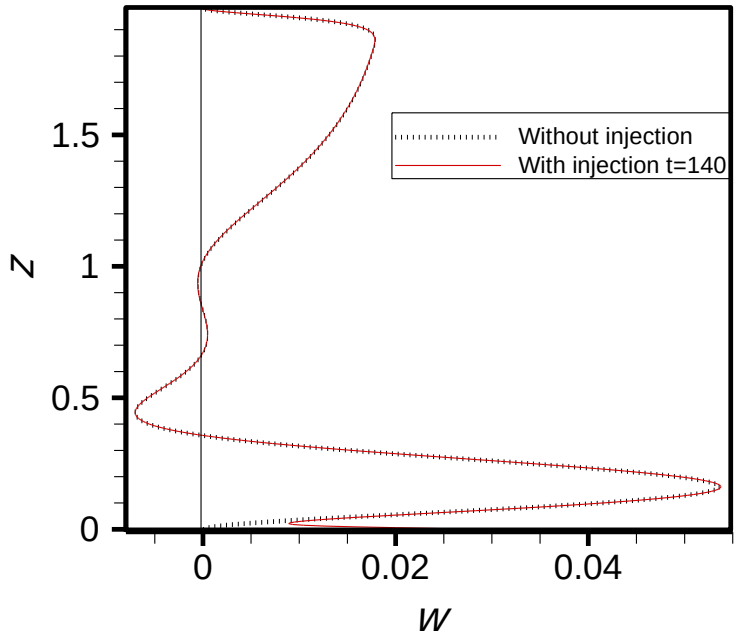

Figure IV.4: Effect of iso-density injection on the axial velocity distribution along the cavity axis; Re=2060

Moreover, several other test cases were carried out by varying the cavity aspect ratio and the disk rotation rate which indicated that the stagnation flow conditions (vicinity of the breakdown region of interest) were not significantly altered so long as the uniform injection velocity was of order of magnitude less than that of the maximum meridian circulation outside the bubble (ambient circulation). The (Re, Λ_h) state diagram of figure IV.5 illustrates the number of current test cases (under iso-density injection) illustrated by distinct symbols on the well-established Escudier's diagram (established experimentally in the absence of injection). It is observed that the current results (symbols) approximately coincide with the stability curves which delimit the regions of breakdown onset

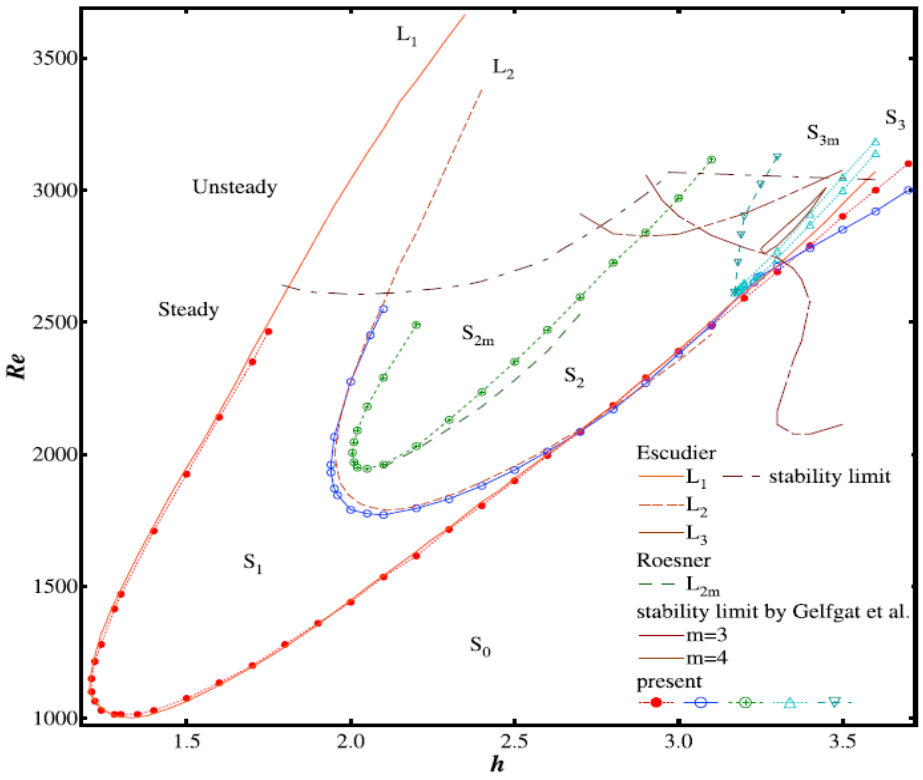

Figure IV.5: Regions of breakdown onset and flow regimes: current results under isodensity injection (*distinct* × symbols) added for comparison to detailed stability diagrams supplied by Iwatsu et al. (absence of injection) [8].

IV.4. Positively buoyant injection $(\Delta\rho/\rho_a = (\rho_j - \rho_a)/\rho_a > 0)$

Motivated by the experimental findings [3] based on flow visualization and in an attempt to provide detailed quantitative results, a numerical investigation is carried out to explore the impact of small density variations of the above confined isothermal swirling flow subjected to a positively buoyant injection, applied at the bottom disk center. We recall that to the best of our knowledge, there has been no prior numerical study of this model helical flow under injection.

To allow direct comparison with the experiments, the sensitivity of breakdown to density variations was first analyzed for the model flow generated in a closed cavity with aspect ratio $\Lambda_h = 1.98$ (fixed in the experiment) and uniform injection rate $U_j = 1.7\times10^{-3} m/s$, while varying the main parameters: the density ratio $\Delta\rho/\rho_a = (\rho_j - \rho_a)/\rho_a$ (ρ_a and ρ_j are densities of the jet and ambient fluid respectively) as well as the rotational Reynolds number defined above.

Besides, the comparison will focus on the flow patterns and corresponding characteristics visualized experimentally at time $t = 110$ (maximum time of observation reported in the experiment). It is worth mentioning that the current work showed that, at this time of observation, the flow didn't yet approached final state.

The current axisymmetric numerical predictions confirmed that very small density differences were sufficient to alter significantly breakdown onset conditions and flow topology. The combined effect of the parameters $(Re,\ \Delta\rho/\rho_a > 0)$ is illustrated in Figure IV.6, covering the ranges $500 < Re < 4000$ and $0\% < \Delta\rho/\rho_a \le 0.02\%$. The particular case $\Delta\rho/\rho_a = 0$, corresponding to the iso-density configuration, is included as a reference case.

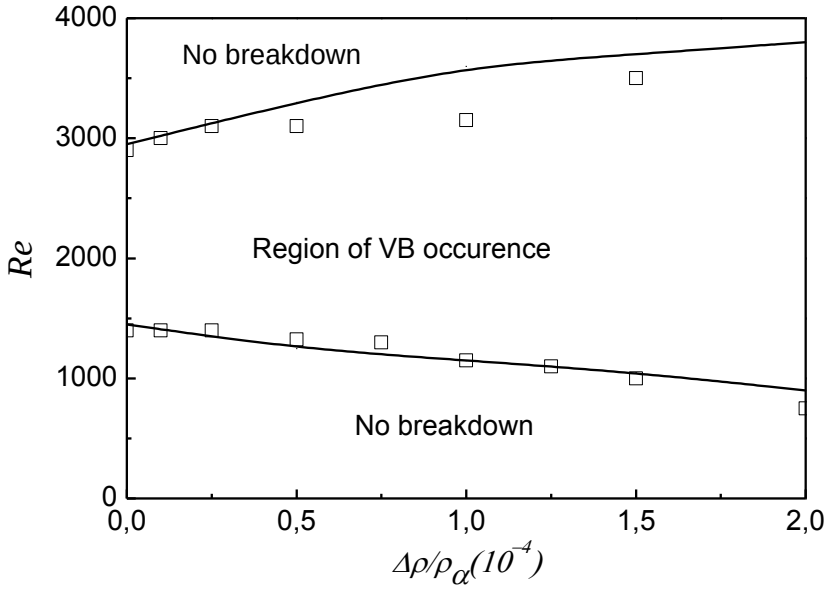

Figure IV.6: $(Re, \Delta\rho/\rho_a > 0)$ state diagram mapping the region of vortex breakdown (VB) occurrence under effect of heavy dye injection. Solid curves are the bounding curves predicted numerically and (□) Symbols denote the corresponding experimental results [3].

The figure displays a state diagram established on the basis of numerous calculations, subjected to the above initial and boundary conditions including selected experimental findings resulting from flow visualization [3]. The results summarize the effect of injecting a fluid slightly heavier than the ambient one, i.e. $\rho_j > \rho_a$. It is observed that both approaches reveal clearly breakdown enhancement with increasing ρ_j .In particular, the region of onset of flow stagnation and associated bubble type reverse flow widens with increasing $\Delta\rho/\rho_a$ and the trend of the corresponding lower bounding curve, which indicates first breakdown onset,

shows a steep and almost linear decrease of the threshold Re with increasing ρ_j. Beyond the upper bounding curve, where the flow is likely to be unsteady as mentioned above, no steady structure is identified. The current numerical predictions are, overall, in good accord with the experimental findings (maximum deviation of order 15% recorded for breakdown onset); despite the apparent significant deviations of the upper bounding curves which may mainly be attributed to the fact that, for the given cavity aspect ratio and over the corresponding range of Re, $Re > 2600$,the flow is likely to be unsteady (bubble axial oscillations were reported in the literature [4,10,11]) which renders the breakdown capture inaccurate . Moreover, the discrepancies may also be related to actual operating conditions (visualization technique and method of breakdown detection) and to the impact of small set up imperfections as discussed in the state of the art.

IV.5. Negatively buoyant injection $(\Delta\rho/\rho_a = (\rho_j - \rho_a)/\rho_a < 0)$

Now, the investigation proceeded to focus on the very light dye injection case $(\rho_j < \rho_a)$. Ismadi et al. [3] reported that, over the time of experimental observation and for the range of parameters: $-0.1\,\% \le \Delta\rho/\rho < 0\,\%$ and $1400 < Re < 3000$, the topology of the bubble type breakdown undergoes significant transition changes but did not disappear with decreasing $\Delta\rho/\rho$. In particular, the structure was observed to evolve and emerge into an off-axis ring type vortex (toroidal type) reminiscent of the breakdown illustrated in figure IV.7 below for the selected density ratio $\Delta\rho/\rho = -0.2\times10^{-3}$ which is supplied by the current simulation. Moreover, this latter phenomenon was reported to occur over the entire range of Re above, when the density ratio varied within the approximate interval $-0.08\,\% \le \Delta\rho/\rho < -0.025\,\%$.

The present numerical predictions, for this model flow, do indeed confirm the bubble transition into a toroidal type vortex (figure IV.8). However, unlike the above experimental counterpart, detailed calculations revealed the existence of a sub range of Re over which the vortex ring itself continued to evolve (beyond the time of experimental observation) until it utterly disappeared; leading to a state which lacks breakdown as clearly illustrated in figure IV.7 for the selected density ratio $\Delta\rho/\rho = -0.4\times10^{-3}$.

At this stage, we conjecture that the limited maximum time of experimental observation may probably be attributed to the dye diffusion which frequently has an impact on the accurate capture of the vortex characteristics.

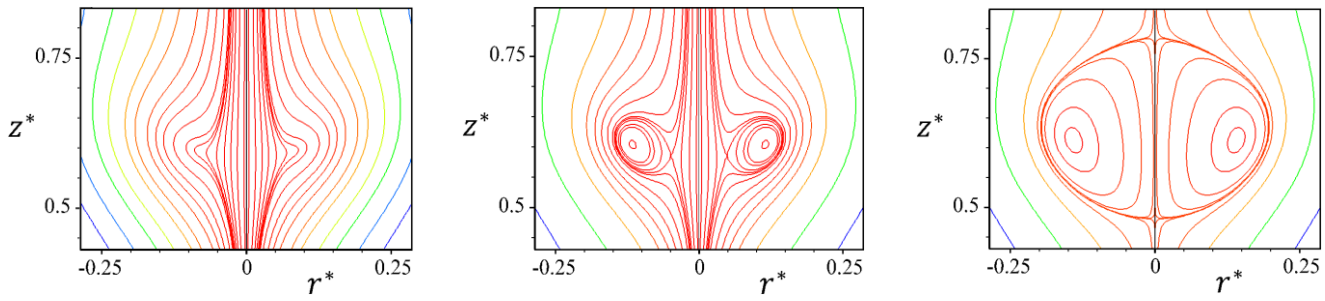

$\Delta\rho/\rho = -0.4\times10^{-3}$ $\Delta\rho/\rho = -0.2\times10^{-3}$ $\Delta\rho/\rho = 0$

Suppression of VB Toroidal (ring type) VB On-axis-Bubble type VB

Figure IV.7: Close up of the steady reverse flow region under effect of negatively buoyant injection $(\rho_j < \rho_a)$; $Re = 1700$, $\Lambda_h = 1.98$ (steady case).

It appeared instructive to also illustrate the onset of the axial breakdown bubble and its bifurcation into a ring type under when the jet injection is lighter than the ambient fluid. The main steps may be described with reference to figure IV.8 below which shows schematically wavy streamlines prior to breakdown, coalescence of the axial stagnation points which delimit the bubble ; causing its detachment into a vortex ring with a saddle point type stagnation point.

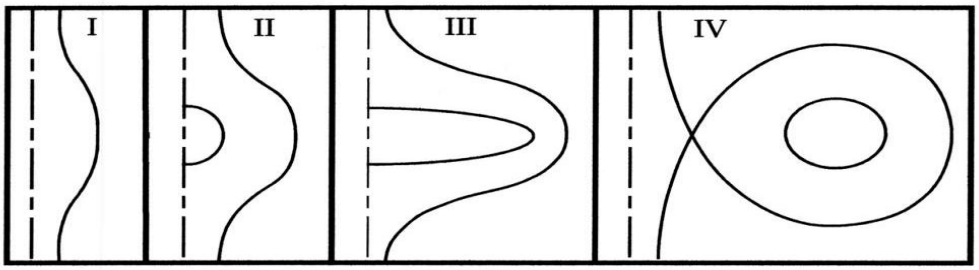

Figure IV.8: Schematic of the process of formation of vortex ring under light dye injection [12]

The current numerical findings are mapped into a $(Re,\ \Delta\rho/\rho < 0)$ phase diagram (Figure IV.9) to allow direct comparison with the experimental counterpart [3]. The mapping in this figure clearly indicates the existence of four distinct regions obtained under light dye injection: one of bubble type occurrence, the second maps out the ring type vortices to which the bubble evolved, in good accord with the experimental findings [3]; finally, two remaining zones

which lack breakdown as a result of decreasing $\Delta\rho/\rho$ which were not invoked and did not appear to have been observed experimentally. This constituted a maximum discrepancy of order 18% on the threshold values of Re .

We conjecture that such a discrepancy may mainly be attributed to the inevitable difference between the well-defined boundary conditions, implemented in axisymmetric simulations, and the effective set up and operating conditions in experiments. In addition, as a result of local dye diffusion, it is worth to mention that some of the provided dye experimental images [3] show bulged regions of concentrated dye which do not accurately capture the required detailed vortex characteristics (saddle points and associated rings are hardly visible).

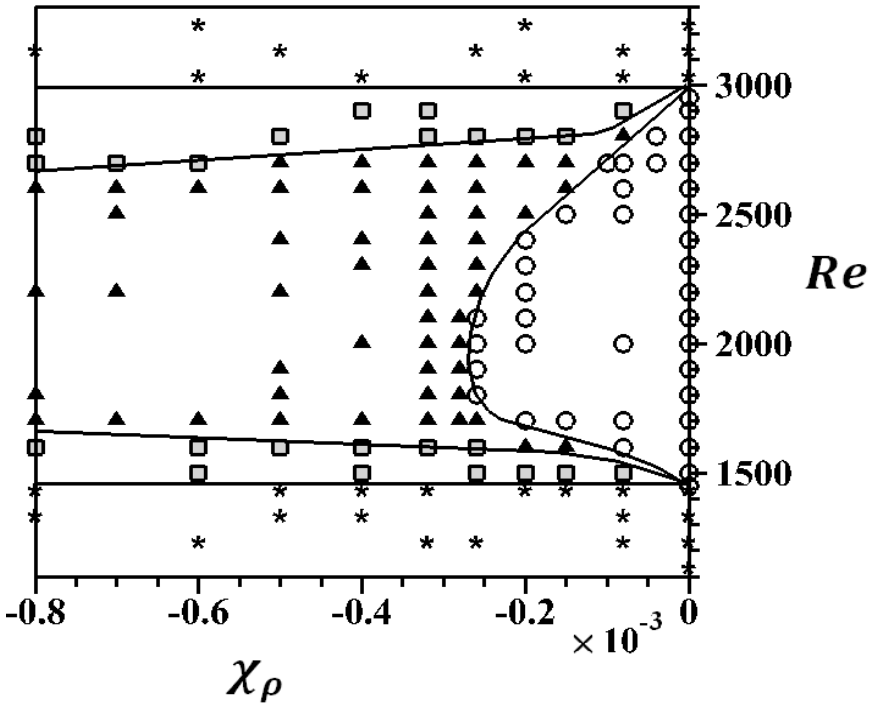

Figure IV.9: (Re, $\Delta\rho/\rho_a < 0$) state diagram, mapping regions of bubble (○) and ring type (▲) vortices under very light dye injection. In contrast to [3], breakdown is suppressed in region with square (□) symbols. (*): region which lacks breakdown.

IV.6. Conclusion

The helical flow generated by the top disk rotation of an enclosed vertical cylinder is studied numerically when subjected to a uniform axial injection of a fluid slightly denser/lighter than the ambient one filling the cavity. In the absence of injection, for given rates of disk rotation and cavity aspect ratio, secondary circulations were evidenced on the cavity axis commonly referred to as bubble type vortex breakdown in accord with experiments. The numerical predictions revealed that the such vortices are very sensitive to small density between the jet and the ambient medium in agreement with experimental findings : denser jet promotes stagnation and vortex formation while lighter jet causes the detachment of the bubble into a vortex ring which may remain robust or disappear , depending upon the range of density ratio and disk rotation rates. Qualitatively, good agreement was found between experiments and the current numerical predictions despite some discrepancies attributed to the set up conditions. Besides, this work complements the experimental findings as it provided additional information on the vortex characteristics difficult to capture.

IV.7. Chapter references

[1] Lim T.T., Cui Y.D.. On the generation of a spiral-type vortex breakdown in an enclosed cylindrical container. Physics of fluids 17, 044105, (2005)

[2] Brøns M., Thompson M.C., Hourigan K.. Dye visualization near a 3D stagnation point: Application to the vortex breakdown bubble. J. Fluid Mech.622, 177–194, (2009)

[3] Ismadi M.Z., Meunier P., Fouras A., Hourigan K., Experimental control of vortex breakdown by density effects, Physics of Fluids, 23**,** 034104 **(**2011)

[4] Meunier P., Hourigan K.. Mixing in a vortex breakdown flow, Journal of Fluid Mechanics, 731, 195-222, (2013)

[5] Quaranta H.U., bolnot h., Leweke T.. Long-wave instability of a helical vortex. J. Fluid Mech. 780, 687–716, (2015)

[6] Verzicco R, Orlandi P. A finite-difference scheme for three-dimensional incompressible flows in cylindrical coordinates. J Comput Phys 1996;123:402–14.

[7] Ruith M.R., Chen P., Meiburg E.. Development of boundary conditions for direct numerical simulations of three-dimensional vortex breakdown phenomena in semi-infinite domains. Computers & Fluids 33, 1225–1250, (2004)

[8] Iwatsu R., Koyama S.A.. A resolution independent solution for confined axisymmetric vortex breakdown flow, Journal of fluid science and technology, 2, 215-225, (2007)

[9] Escudier M.P.. Observations of the flow produced in a cylindrical container by a rotating end wall, Exp. Fluids 2, 189-196, (1984)

[10] Lopez J.M., Perry A.D.. Axisymmetric vortex breakdown, Part 3, Onset of periodic flow and chaotic advection, Journal of Fluid Mechanics, 234, 449-471, (1992)

[11] Gelfgat A.Y., Bar-Yoseph P.Z., Solan A.. Three-dimensional instability of axisymmetric flow in a rotating lid-cylinder enclosure, Journal of Fluid Mechanics, 438, 363–377, (2001)

[12] Husain H.S., Shtern V., Hussain F.. Control of vortex breakdown by addition of near-axis swirl, Physics of Fluids 15, 271-279, (2003)

EFFECT OF THERMAL BUOYANCY ON CONFINED VORTEX FLOWS

V.1. Introduction

Motivated by the main numerical findings of the previous chapter, devoted to the vortex characteristics of isothermal swirling flows under very small density variations, it appeared natural to raise the question of the equivalent model flows which, in practical applications, may inevitably undergo small temperature variations. This issue was first noted by Billant et al. [1] who explored experimentally the structure of isothermal unconfined (free) swirling jets and found it very sensitive to the experimental conditions. This was later confirmed by Dina et al. [2] who extended the investigation to include small temperature variations between the free jet core and the ambient fluid.

V.2. Geometry and control parameters

In this chapter, thermal buoyancy is introduced by two means (figure V.1) and applied to the confined helical flows studied numerically in the previous chapter. First, the numerical investigation considers the model flows generated within a vertical cylinder with a single disk rotation subjected to warm/cool axial injection. Then, a second configuration is considered which consists of the same basic helical flow, without injection, with buoyancy induced by a warm/cool small rod placed at the fixed disk center.

- **Control parameters**

At this stage, it is worth recalling the main parameters which govern the flow dynamics under consideration, induced by the combined kinematic and thermal effects; namely, the rotational Reynolds, the cavity aspect ratio and the Richardson number which appropriately accounts for thermal buoyancy strength, defined respectively as:

$$Re = \frac{\Omega R^2}{\upsilon}, \Lambda_h = \frac{H}{R}, Ri = \frac{\beta g \Delta T}{\Omega^2 R}$$

where $\Delta T = T_j - T_a$ is the temperature gradient between the axial jet (or the rod) and the ambient fluid, υ and β denote the kinematic viscosity and thermal expansion coefficients respectively.

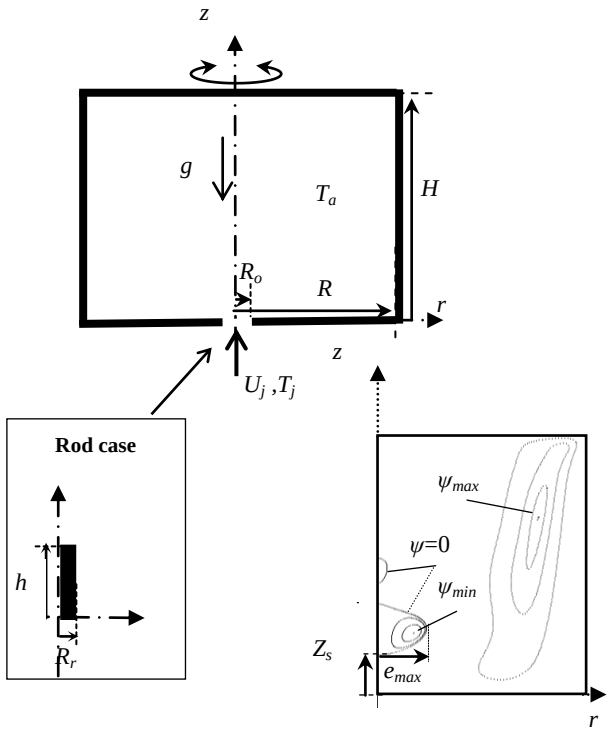

Figure V.1: Schematic of the geometry and numerical domain which displays a meridian streamline pattern with an on-axis two bubble type breakdown and selected vortex characteristics : Z_s (upstream stagnation point), $e_{\max}$ (bubble radial extent), stagnation line $\psi = 0$ maximum volumetric flow rates inside ($\psi_{\min} < 0$) and outside ($\psi_{max} > 0$) the vortex.

V.3. Basic flow under neutrally buoyant injection

Prior to investigating thermal effects, it appeared necessary to first consider the case under isothermal injection (neutrally buoyant injection $Ri = 0$) in order to assess the sensitivity of the vortex pattern to the inlet geometry and associated injection conditions. Figure V.2 shows a close up of the meridian vortex pattern, before and after neutral injection applied to the configuration $(\Lambda_h, Re) = (1.98, 1700)$; assuming experimental conditions [3,4]: uniform injection velocity $U_j = 1.7 \times 10^{-3} m/s$ at the orifice (radius ratio $\delta_o = R_o / R = 7.69 \times 10^{-3}$). The figure reveals mainly a slight divergence of the selected streamlines in the vicinity of the axis, indicating a very weak flow deceleration downstream the vortex; causing a minor upward shift of the downstream stagnation point P_r $(<1\%)$. However, these changes did not impact significantly the vortex topology and maximum vortex intensity $(|\psi_{\min}|)$.

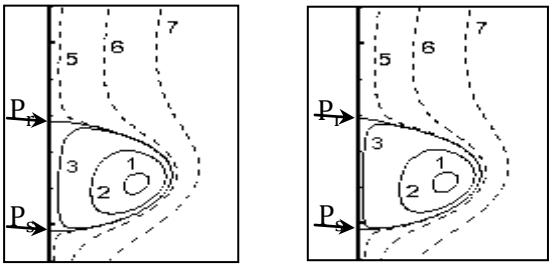

(a) **(b)**

Figure V.2: A close up of an on-axis vortex (solid lignes) in the meridian plane $[0,r[\times[0,z[$. (a) no injection and (b) under isothermal injection. P_s and P_r are the upstream and downstream stagnation points respectively.

V.4. Effect of thermally buoyant injection

In this section we focus on the case when the vortex flows are subjected to buoyancy, induced by uniform injection at temperatureT_j slightly different from the ambient fluid temperatureT_a . The inlet conditions are the same as those implemented in the case of a neutrally buoyant injection $(Ri=0)$ described above. Buoyancy strength is controlled by varying the Richardson number Ri over a range corresponding to small temperature gradients. Calculations were performed over the parameter ranges $250 \le Re \le 2600, 0.8 \le \Lambda_h \le 2.5, -0.023 \le Ri \le 0.092$

V.4.1. Warm injection

When the jet temperature is slightly higher than that of the ambient fluid $(Ri>0)$, calculations revealed significant changes of the flow pattern due to buoyancy. In particular, it was found numerically that a gradual increase of the jet temperature caused the suppression of the axial flow stagnation but the vortex breakdown didn't disappear for given range of parameters: the bubble bifurcates into a ring type vortex (toroidal vortex). As expected, this result is in good qualitative agreement with the light dye injection case visualized experimentally by Ismadi et al. [3] as depicted by the comparison of the vortex structure of figure V.3 for the selected parameters $(Re,\Lambda_h,Ri)=(2423,1.98,0.023)$.

While the experiments were performed for a single case of cavity aspect ratio, the present calculations were carried out for various parameters in order to confirm the findings. In a

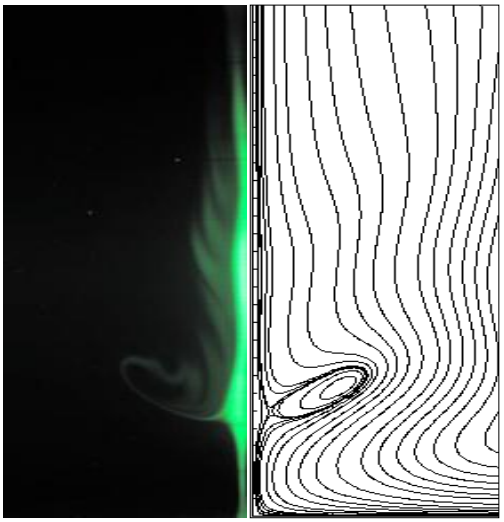

Figure V.3: A ring type vortex induced by warm injection (meridian streamlines at the right) and experimental dye visualization (left) [3]; $(Re, \Lambda_h, Ri) = (2423, 1.98, 0.023)$

search for additional information on the vortex characteristics, it was found numerically that the robustness of the vortex ring described above depended the parameter ranges used: it may remain robust and observable or may continue to evolve in time until it utterly disappears; leading to a state which lacks breakdown. Indeed, this can be remarked by analyzing, for instance, the selected configuration $(Re, \Lambda_h) = (1700, 1.98)$ for different values of the Richardson number as illustrated in figure V.3 which includes the neutrally buoyant case $Ri = 0$ (Figure V.2) as a reference case.

The figure shows that the bubble initially located along the cavity axis (isothermal case $Ri = 0$) evolved into a toroidal type structure under effect of warm injection for the case $(Re, \Lambda_h, Ri) = (1700, 1.98, 0.023)$ which remains robust and observable for all times. The associated close up figure clearly illustrates the detached structure with a saddle point at its periphery (stagnation circle if one considers the entire cavity). However, by varying Ri over the range $0 \le Ri \le 0.092$, for fixed aspect ratio and Re, detailed timewise evolution of the flow field revealed numerically the existence of a limited sub-region, involving relatively lower Re values (state diagrams in the next section) where the ring type vortex itself continued to

evolve by shrinking until it utterly disappeared; probably as a result of viscous damping. This trend is readily apparent in Figure V.4.c for $(Re, \Lambda_h, Ri) = (1700, 1.98, 0.046)$, showing a bulged region (swelling streamlines) which lacks breakdown. Besides, this numerically predicted flow evolution was found to occur for various couples of parameters (Re, Λ_h, Ri) as discussed in the next section.

However, the experimental counterpart [3], performed for a single cavity aspect ratio, reported the bubble transition toward the ring type vortex but did not invoke the particular cases of its suppression; although one would expect, approximately, very similar trends as regards to the very small density variations involved in both studies. Analogous discrepancies between dye experiments on confined vortex breakdown and numerical predictions were reported by Herrada et al. [5,6]. We conjecture that such a discrepancy may mainly be attributed to the inevitable difference between the well-defined boundary conditions implemented in the frame work of axisymmetric simulations and the effective set up and operating conditions in experiments [7,4]. In addition, as a result of local dye diffusion, experimental images [8,3,4,9] show frequently bulged regions of concentrated dye which do not accurately capture the required detailed vortex characteristics (saddle points and associated rings are hardly visible).

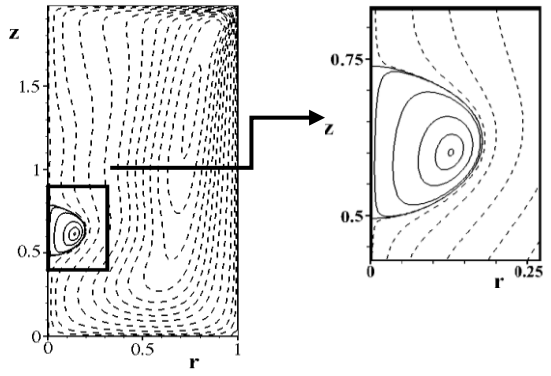

(a) $Ri = 0$ **(a')** $Ri = 0$

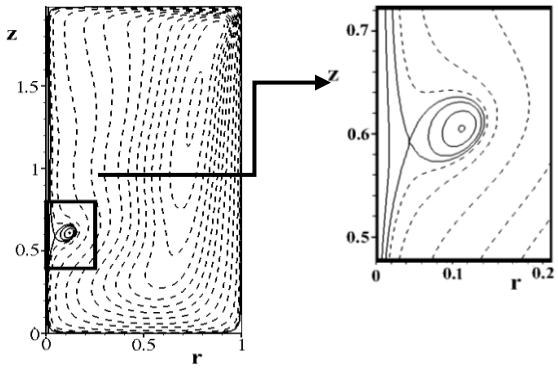

(b) $Ri = 0.023$ (b') $Ri = 0.023$

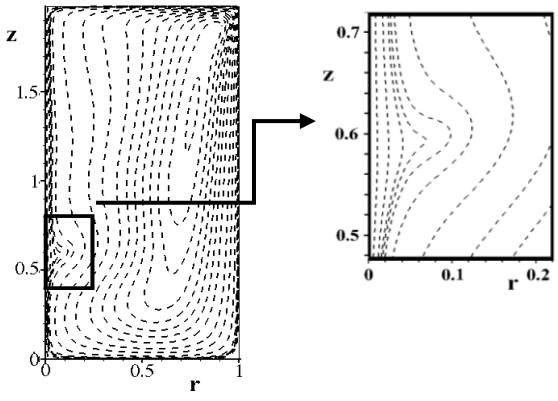

(c) $Ri = 0.046$ (c') $Ri = 0.046$

Figure V.4: (a), (b), (c): flow pattern under effect of warm injection; $Re = 1700$, $\Lambda_h = 1.98$ for three selected values of Ri as indicated above; (a'), (b'), (c') : a close up of the corresponding reverse flow regions respectively.

- **Combined effect of parameters** $(Re, Ri > 0)$

The above findings are extended to explore the combined influence of the rotational Reynolds number and the buoyancy parameter Ri $(Ri > 0)$. Results are summarized in the $(Re, Ri > 0)$ state diagram (Figure V.5), established on the basis of detailed calculations carried out over the parameters ranges $1400 \le \mathrm{Re} \le 2600$ and $0 \le Ri \le 0.092$, for fixed cavity aspect ratio $\Lambda_h = 1.98$ and two time stations: the higher time approaches steady state and the lower one was selected as a reference time. We recall that for $Re < 1400$, the basic flow lacks breakdown.

The mapping identifies three distinct flow regimes with bounding curves, brought about by thermal effects. In particular, a region of bubble type (which shrinks with increasing time), another of robust toroidal eddy structure (which expands with time) and finally one which lacks breakdown, involving relatively lower Re values and therefore more viscous damping. For fixed Re over the range $1400 < Re \le 1750$, it is remarked that the bubble type vortex disappears under warm injection and the corresponding bounding curve is almost linear over the sub-range $0 < Ri < 0.018$. Outside this latter interval, i.e. $0.018 < Ri \le 0.092$, variations are much less pronounced. We recall that the above numerical predictions showed that the bubble detached from the axis prior to its suppression. However, the remaining range $1700 < Re < 2600$ reveals that bubble bifurcation into a steady eddy structure, which remains observable, with increasing Ri .

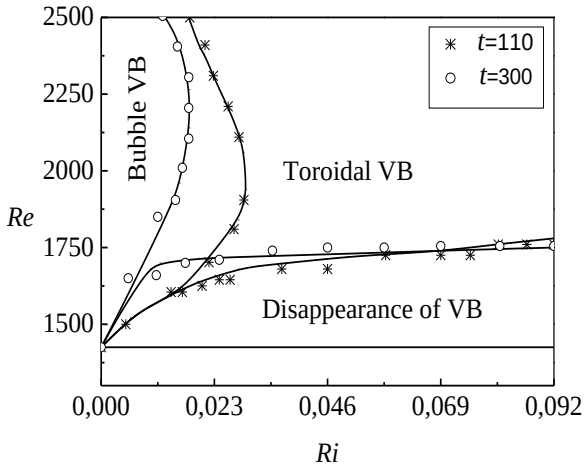

Figure V.5: $(Re, Ri > 0)$ diagram for two selected times. As Ri increases vortex breakdown (VB) evolves into a toroidal pattern which may remain observable or disappear.

The bounding curve, in this case, is almost linear over the approximate sub-range $1400 < Re < 2000$. Outside this latter range a decrease of Ri is remarked with increasing Re; indicating higher sensitivity of the bubble to the buoyant injection.

V.4.2. Cool injection

The model flow under cool injection $(Ri < 0)$, is described in this section. Unlike the previous case, buoyancy is shown here to promote flow stagnation conditions as well as vortex strength and size. This is evidenced in Figure V.6, for the selected couple of parameters $(Re, \Lambda_h, Ri) = (1700, 1.98, Ri < 0)$, which shows qualitatively, a more axially elongated and radially extended flow reversal than that resulting from the neutrally buoyant configuration. Besides, no ring type pattern was observed in this case.

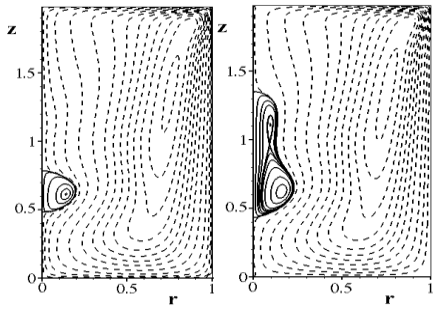

$Ri = 0$ $Ri = -0.023$

Figure V.6: Meridian streamlines illustrating effects of cool injection $(Ri < 0)$;

$(Re, \Lambda_h, Ri) = (1700, 1.98, -0.023)$

V.4.3. The role of the axial pressure

It is well established in the literature that bubble type breakdown onset is associated to the existence of an adverse pressure gradient (relative to the flow direction) which causes the flow to stagnate and reverses its direction. So, it is instructive to examine pressure distribution along the centerline prior and after implementing the control strategies. In figure V.7 (which includes a zoom of the vicinity of the core region of interest), the pressure coefficient distribution along the cavity axis is plotted in the case of warm and cool injection along with the reference isothermal configuration which is shown above to display bubble type breakdown. It is observed that the pressure coefficient increases with increasing jet

temperature which tends to prevent stagnation while the inverse is remarked when is decreased (decrease of c_p ($c_p < 0$)).

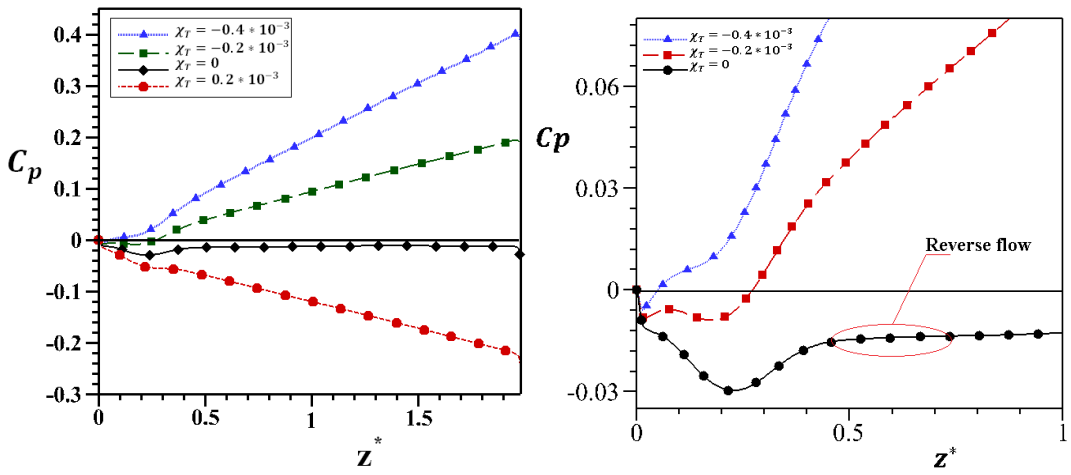

Figure V.7: Distribution of the pressure coefficient on the cavity axis corresponding to the steady flow pattern induced for $Re = 1700$, $\Lambda_h = 1.98$.

V.4.4. (Re, Λ_h) and (Re, Ri) state diagrams

To further highlight the distinct and combined roles of the geometric and dynamic parameters involved, it appeared instructive and convenient to discuss the new (Re, Λ_h) and (Re, Ri) diagrams.

The effect of the cavity aspect ratio is illustrated in (Figure V.8) for $0.8 \le \Lambda_h \le 2.5$, $250 \le Re \le 2600$ and two selected Ri values; including the neutrally buoyant case $Ri = 0$ for comparison. For fixed Λ_h, the lower (upper) curve defines the critical Re for breakdown onset (suppression). The case $Ri = 0$ (under injection) is approximately similar to the well documented configuration without injection [10]. Under a weak cool injection, the breakdown zone is shown to expand and cover wider ranges of (Re, Λ_h). In particular, the lower bounding curves indicate a significant reduction of the threshold Re (up to 50% reduction) for breakdown onset: much lower top disk rotation rates are sufficient to trigger flow stagnation. Besides, it is well established that configurations without injection display breakdown only if $\Lambda_h > 1.3$ [10,11,9]. In contrast, this limit is shown to reduce considerably when the flow is subjected to cool injection, as depicted in Figure8 over the range $0.8 \le \Lambda_h \le 1.3$.

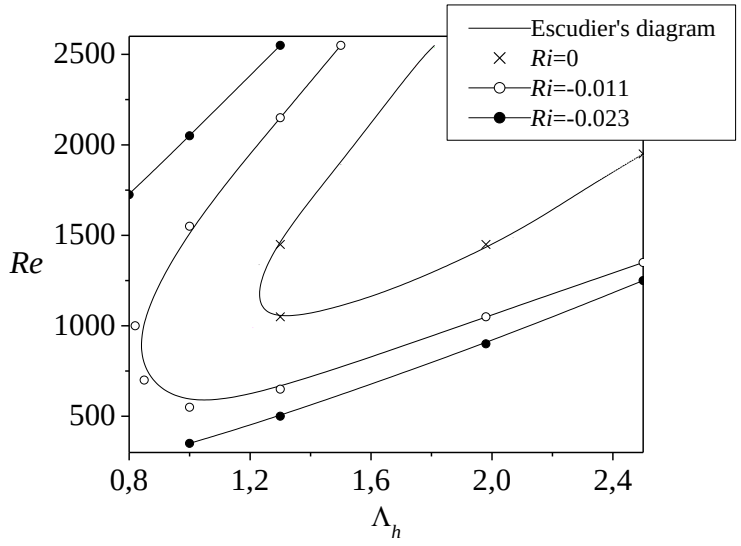

Figure V.8: (Re, Λ_h) Diagram mapping the breakdown region (bounded by an upper and lower curve) for three selected $Ri < 0$ values. Cool injection enhances breakdown.

Next, is discussed the sensitivity of breakdown to the combined variation of Re and Ri, for different aspect ratios; focusing on the impact of weak thermal buoyancy. Figure V.9 illustrates a (Re, Ri) diagram covering the ranges $250 \le Re \le 2600$, $-0.023 \le Ri \le 0.023$ and for five distinct aspect ratios $\Lambda_h = 1, 1.3, 1.64, 1.98$ and 2.5; including the neutrally buoyant injection case $(Ri = 0)$ for the sake of comparison. It is clearly observed that $Ri > 0$ delays the flow stagnation as illustrated by the slight increase of the threshold Re_c (by approximately 10%) for $\Lambda_h > 1.3$. However, weak buoyant cool injection $(Ri < 0)$, for all aspect ratios considered, is sufficient to promote breakdown occurrence as indicated by the steep decrease of the corresponding Re_c bounding curves. The threshold Re may drop by approximately 70% as depicted by comparing the trend of the lower curve corresponding to $\Lambda_h = 1$ between the points $(Re \approx 1000, Ri \approx -0.04)$ and $(Re \approx 300, Ri \approx -0.023)$. Besides, It is remarked that under cool injection and over the range of Re considered,

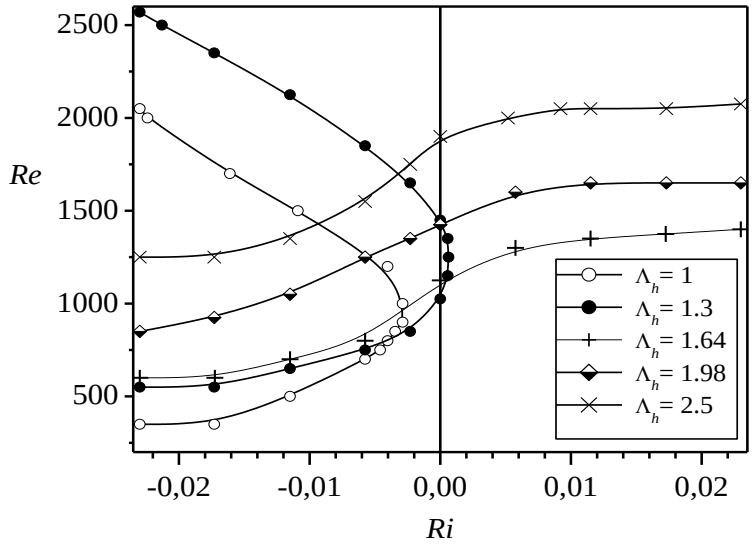

Figure V.9: (Re, Ri) diagram for five aspect ratios, indicating breakdown occurrence under warm $(Ri > 0)$ and cool $(Ri < 0)$ injection: for $\Lambda_h = 1$ and $\Lambda_h = 1.3$ breakdown bounded by an upper and lower curve while for higher aspect ratios it occurs above a single curve (breakdown threshold).

cavities with $\Lambda_h = 1$ and $\Lambda_h = 1.3$ display breakdown in the inner region bounded by two curves while only a single threshold curve (lower bound) is illustrated for the three remaining relatively higher aspect ratios; the corresponding upper limit, if it exists, would probably occur over the range of oscillatory regime.

V.4.5. The role of the local swirl number

Breakdown in the disk-cylinder with spinning lid may be associated to the competition between two main local characteristics of the helical jet flow which develops within the viscous core region along the cavity axis [12,13] namely the swirl strength and the meridian flow intensity characterized respectively by the local rotational and axial Reynolds numbers: $\mathrm{Re}_r = v_m^* r_c^* / \upsilon \left(\mathrm{Re}_r = v_m r_c \,\mathrm{Re}\right), \mathrm{Re}_a = w_m^* r_c^* / \upsilon \left(\mathrm{Re}_a = w_m r_c \,\mathrm{Re}\right)$ where variables with a star denote dimensional quantities. Here, $w_m = w_{\max}(0, z_m)$ is the maximum axial velocity reached at $z = z_m$ along the cavity axis and $v_m = v_{\max}(r_c, z_m)$ the maximum swirl velocity attained at the axial level $z = z_m$ and radial extent $r = r_c$ which defines the viscous core edge.

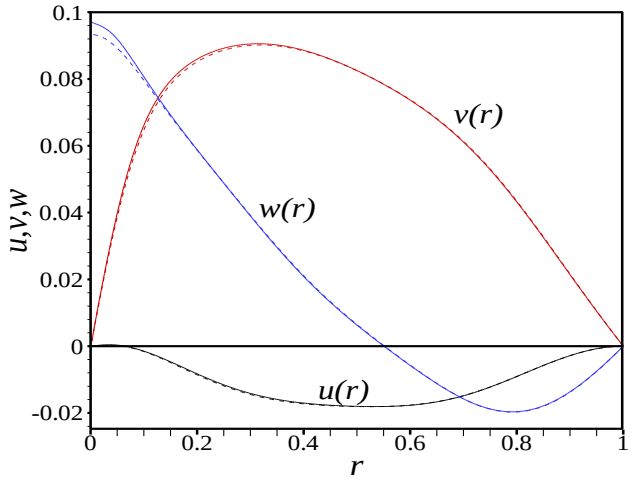

Figure V.10: Radial distribution of the velocity field at $z_m = 0.26$ corresponding to the configuration $\mathrm{Re} = 2060$, $\Lambda_h = 2.5$, $Ri = 0.023$ (solid curves) and $Ri = 0$ (broken curves).

Accordingly, a consistent local parameter to analyze breakdown development may therefore be constructed as the ratio $S_N = \mathrm{Re}_r / \mathrm{Re}_a$, which defines the local swirl number [12]. As a test case, the variation of S_N is evaluated approximately in order to predict the sensitivity of the flow to warm injection for the selected configuration $\mathrm{Re} = 2060$, $H / R = 2.5$ which displays two on-axis breakdown when $Ri = 0$ [11,14,9]. Calculations for this case indicated $z_m = 0.26$, and the corresponding radial distribution of the velocity field (Figure V.10) provided $S_N = v_m / w_m \approx 0.97$ when $Ri = 0$, in agreement with recent numerical predictions [12]. Now, under warm injection $(Ri = 0.023)$ a small increase of w_m is remarked due to buoyancy (the two remaining velocities are almost unaltered), which subsequently causes flow acceleration of weak intensity but sufficient to suppress breakdown. This effect corresponds to a swirl number reduction $(S_N \approx 0.93)$ just below the swirl strength required for breakdown onset. Besides, it can be remarked that the radial velocity magnitude is relatively small and its contribution to the local swirl number can be neglected.

V.5. The rod configuration under differential heating

In an attempt to confirm buoyancy influence on the stagnation flow conditions, the study was extended to consider a different set up which generates buoyancy by means of a differentially heated /cooled tiny rod sealed to the bottom disc center of the cylinder. Such a configuration and associated conditions are more amenable to numerical modeling and relatively easier to implement in practice.

This configuration introduces a modified Richardson number based on the rod temperature (T_{rod}) which replace (T_j). Besides, the rod radius R_r is chosen to fit the orifice radius R_0 used in the injection case above $(R_r = R_0)$ which yields equal ratio $\delta_r = R_r / R = \delta_0$ ($\delta_o = 7.69 \times 10^{-3}$ [13]). In order to obviate the occurrence of undesired additional eddies occurring at the rod tip which may alter breakdown onset conditions, we set the rod aspect ratio to $\delta_h = R_r / h = 0.25$ .Under such geometrical characteristics the presence of the rod did not alter significantly the vortex flows characteristics prior to differential heating and so may be regarded as a non intrusive means of flow control. Qualitatively, the numerical predictions revealed that small temperature gradients corresponding to the range $-0.116 \le Ri \le 0.116$, applied between the rod and the ambient fluid, were sufficient to alter significantly the vortex patterns. In particular, when the rod temperature is set slightly higher than that of the ambient fluid $(Ri > 0)$ a buoyancy force is generated, inducing an upward convection of swirling co-flow, of week intensity but sufficient to enhance the axial flux and angular momentum transfer, which act to prevent flow stagnation and associated vortex formation. This is depicted qualitatively, for $\Lambda_h = 1.98$, $Re = 1700$ and for the selected value $Ri = 0.116$, by the non-uniformly spaced meridian streamlines (Figure V.11.b); the case $Ri = 0$ (Figure V.11.a) corresponds to the isothermal configuration. In contrast, when the rod is differentially cooled, an enhancement of the bubble size and occurrence of a second reverse flow structure were obtained (Figure V.11.c).

In addition, to allow comparison of the threshold buoyancy parameter Ri required for breakdown suppression, in both rod and injection models, the axial velocity distribution at the cavity axis is supplied (Figure V.12), before and after thermal control, when $Re = 1700, \Lambda_h = 1.98$. The figure confirms that, prior to differential heating, both means induce local effects without altering significantly the flow stagnation location. However, for a fixed ambient fluid temperature, to suppress breakdown by means of the rod differential heating, a temperature gradient $\Delta T = T_{rod} - T_a = 5K$ $(Ri = 0.116)$ was required and no transient ring type vortex was found to occur. In contrast, calculations in the case of the injection model revealed that $\Delta T = 1K$ $(Ri = 0.023)$ caused the detachment of the axial bubble which evolved into a robust steady ring type vortex while $\Delta T = 2K$ led a state which lacks breakdown.

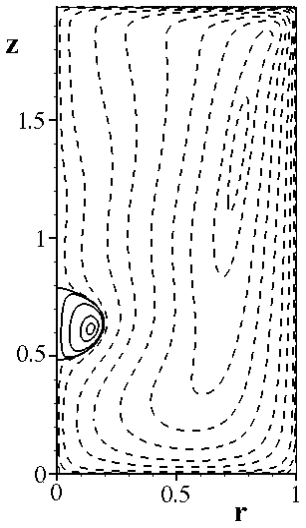

(a) $Ri = 0$

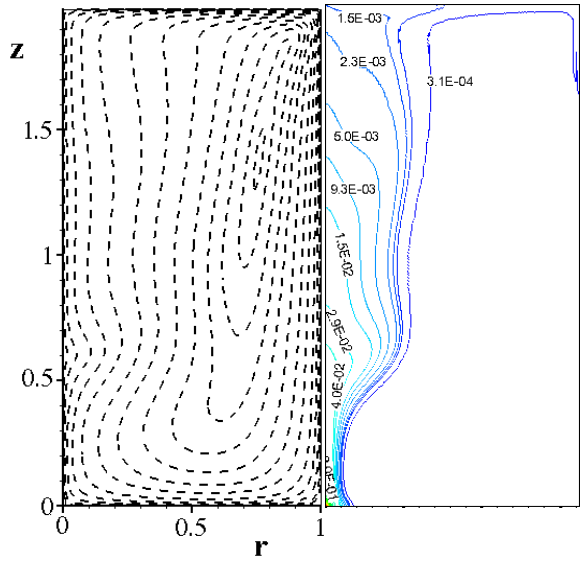

(b) $Ri = 0.116$

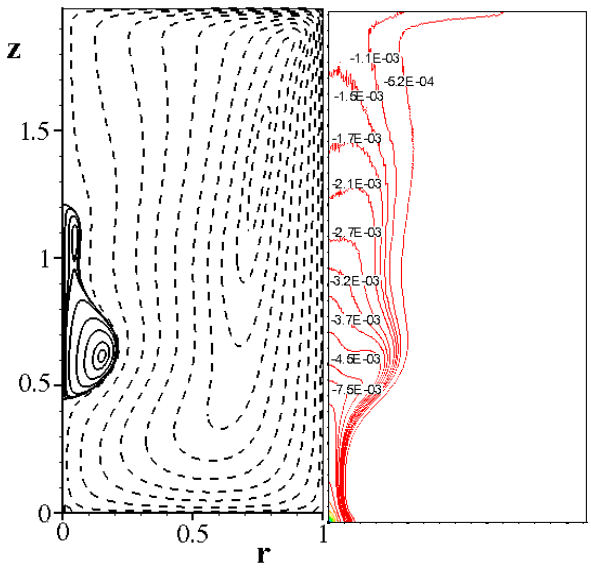

(c) $Ri = -0.116$

Figure V.11: Meridian flow pattern subjected to differentially heated/cooled rod; streamlines at the left and the right contour lines of isotherms; $Re = 1700, \Lambda_h = 1.98$

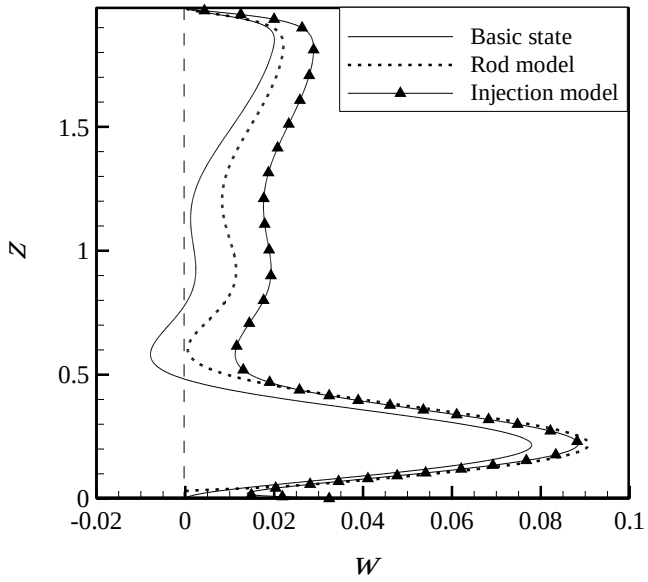

Figure V.12: Axial velocity distribution corresponding to the critical Ri required to suppress breakdown: $Ri = 0.116$ (rod case) and $Ri = 0.046$ (injection case); $Re = 1700$, $\Lambda_h = 1.98$

V.6. Conclusion

Thermal buoyancy, implemented by means of warm/cool uniform injection or by a differentially heated tiny rod, was shown numerically to constitute an effective means of controlling axial flow stagnation and associated breakdown in a disk-cylinder system with a rotating lid. In particular, warm (cool) injection or differentially heated (cooled) rod, applied upstream the vortex, were found to both prevent (favor) breakdown. In addition, under warm injection, buoyancy was found to suppress on-axis stagnation points while the associated bubble bifurcates into an off-axis vortex ring which may remain robust and observable or may continue to evolve until it disappears; depending on buoyancy strength and viscous damping effects. These findings were established for various $(\Lambda_h, \mathrm{Re}, Ri > 0)$ parameters. Besides, the differentially heated/cooled tiny rod configuration, considered as a non-intrusive means based on thermal stratification was found to alter significantly the conditions of breakdown onset but, unlike the injection model, did not exhibit any ring type vortex. The current findings, which may be useful for bioreactors, constitute a platform for further investigations which, in perspective, explore oscillatory regimes.

V.7. Chapter references

[1] Billant P., Chomaz J., Huerre P., Experimental study of vortex breakdown in swirling jets, Journal of Fluid Mechanics, 376, p. 183-219, (1998)

[2] Dina M., and Jacob C. The effect of buoyancy on vortex breakdownin a swirling jet. J. Fluid Mech. vol. 571, 177–189, (2007)

[3] Ismadi M.Z., Meunier P., Fouras A., Hourigan K., Experimental control of vortex breakdown by density effects, Physics of Fluids, 23**,** 034104 **(**2011)

[4] Meunier P., Hourigan K.. Mixing in a vortex breakdown flow, Journal of Fluid Mechanics, 731, 195-222, (2013)

[5] Herrada, M. A., &Shtern, V. Control of vortex breakdown by temperature gradients. Physics of Fluids, 15, 3468–3477, (2003a)

[6] Herrada, M. A., and Shtern, V. Vortex breakdown control by adding near-axis swirl and temperature gradients. Physical Review E, 68, 041202, (2003b)

[7] Brons M., Shen W.Z., Sorensen J.N., Zhu W.J.. The influence of imperfections on the flow structure of steady vortex breakdown bubbles, Journal of Fluid Mechanics, 578, 453-466,(2007)

[8] Omi, Y., & Iwatsu, R. Numerical study of swirling flows in a cylindrical container with co-/counter-rotating end disks under stable temperature difference. International Journal of Heat and Mass Transfer, 48, 4854–4866, (2005)

[9] Iwatsu R., Koyama S.A.. A resolution independent solution for confined axisymmetric vortex breakdown flow, Journal of fluid science and technology, 2, 215-225, (2007)

[10] Lopez J.M.. Axisymmetric vortex breakdown, Part 1, confined swirling flow, Journal of Fluid Mechanics 221, 533-552, (1990)

[11] Escudier M.P.. Observations of the flow produced in cylindrical container by a rotating endwall. Exp. Fluids 2, 189-196, (1984)

[12] Jones M.C., Hourigan K., Thompson M.C.. A study of the geometry and parameter dependence of vortex breakdown. Physics of Fluids, 27, 044102, (2015)

[13] Moise P., Mathew J..Bubble and conical forms of vortex breakdown in swirling jets, Journal of Fluid. Mechanics 853, 322-357, (2019)

[14] Dennis D.J.C., Seraudie C., Poole R.J.. Con-trolling vortex breakdown in swirling pipe flows: Experiments and simulations, Physics of Fluids 26 (5) 053602, (2014)

GENERAL CONCLUSION

The helical flow which displays axisymmetric on-axis breakdown, driven by the top end wall rotation of a confined cylindrical enclosure filled with an incompressible fluid, is simulated numerically.

Firstly, interest focused on the sensitivity the vortex feature when subjected to a uniform axial injection of a dense/light fluid. In the absence of injection, for given rates of disk rotation and cavity aspect ratio, secondary circulations were evidenced on the cavity axis commonly referred to as on-axis bubble type vortex breakdown in very good accord with experiments and previous numerical works. The numerical predictions revealed that such vortices are very sensitive to small density variation between the jet and the ambient medium in agreement with recent experimental findings: denser jet promoted stagnation and vortex formation while lighter jet caused the detachment of the bubble into a toroidal vortex which may remain robust or disappear; depending on the range of density ratio and disk rotation rates. Qualitatively, the flow topologies and structures resulting from the current numerical predictions were in good agreement with those visualized in experiments, despite some discrepancies which may presumably be attributed to the set up and operating conditions. Besides, although the current isothermal simulation does not supplement its experimental counterpart, it nevertheless provided additional information on detailed characteristics not clearly observed and captured in the reported experiments.

Secondly, a new configuration was considered which explored the effects of thermal buoyancy implemented by means of warm/cool uniform injection or by a differentially heated tiny rod. This new approach was shown numerically to constitute an effective means of breakdown control. In particular, warm (cool) injection or differentially heated (cooled) rod, applied upstream the vortex, were found to both suppress (promote) breakdown. In addition, under warm injection, buoyancy was found to prevent the occurrence of on-axis stagnation points without eliminating breakdown. In fact, results revealed that the associated bubble detaches from the axis and bifurcates into an off-axis vortex ring which may remain robust and observable or may continue to evolve until it utterly disappears; depending on buoyancy strength and viscous damping effects. These findings were established for various $(\Lambda_h, Re, Ri > 0)$ parameters.

Finally, thermal effects were investigated by means of differentially heated/cooled tiny rod, considered as a non intrusive means based on thermal stratification and natural

convection. This configuration was found to alter significantly the conditions of breakdown onset but, unlike the injection model, did not exhibit any ring type vortex.

The current findings, which may be useful for bioreactors, constitute a platform for further investigations which, in perspective, may be extended to account for the more complex non-axisymmetric structures and explore oscillatory regimes. Besides, the above evidence on the sensitivity of the vortex flows to very small buoyancy perturbations, highlighted the need to handle very carefully the operating conditions and set ups in experiments (especially when dye is used for visualization).